



Quantitation of dynamic total-body PET imaging: recent developments and future perspectives

Fengyun Gu^{1,2} · Qi Wu²

Received: 22 December 2022 / Accepted: 5 June 2023 / Published online: 18 July 2023
© The Author(s) 2023

Abstract

Background Positron emission tomography (PET) scanning is an important diagnostic imaging technique used in disease diagnosis, therapy planning, treatment monitoring, and medical research. The standardized uptake value (SUV) obtained at a single time frame has been widely employed in clinical practice. Well beyond this simple static measure, more detailed metabolic information can be recovered from dynamic PET scans, followed by the recovery of arterial input function and application of appropriate tracer kinetic models. Many efforts have been devoted to the development of quantitative techniques over the last couple of decades.

Challenges The advent of new-generation total-body PET scanners characterized by ultra-high sensitivity and long axial field of view, i.e., uEXPLORER (United Imaging Healthcare), PennPET Explorer (University of Pennsylvania), and Biograph Vision Quadra (Siemens Healthineers), further stimulates valuable inspiration to derive kinetics for multiple organs simultaneously. But some emerging issues also need to be addressed, e.g., the large-scale data size and organ-specific physiology. The direct implementation of classical methods for total-body PET imaging without proper validation may lead to less accurate results.

Conclusions In this contribution, the published dynamic total-body PET datasets are outlined, and several challenges/opportunities for quantitation of such types of studies are presented. An overview of the basic equation, calculation of input function (based on blood sampling, image, population or mathematical model), and kinetic analysis encompassing parametric (compartmental model, graphical plot and spectral analysis) and non-parametric (B-spline and piece-wise basis elements) approaches is provided. The discussion mainly focuses on the feasibilities, recent developments, and future perspectives of these methodologies for a diverse-tissue environment.

Keywords Total-body PET · Multiple organs · Arterial input function · Kinetic models · Parametric imaging

Introduction

In recent years, positron emission tomography (PET) has a wide range of clinical and research applications in oncology, cardiology, and neurology [1, 2]. It is a unique imaging modality that enables the measurements of a diverse range of functional and biological processes (e.g., tumor metabolism

[3], proliferation [4], blood flow [5], and receptor-binding [6]), depending on the administered radiotracer. In daily clinical practice, PET imaging is obtained at a single time point and assessed visually or using simple indices, e.g., standardized uptake value (SUV) [7]. Although these are sufficient for many diagnostic applications, dynamic scans with multiple time frames are implemented in some research avenues for advanced diagnosis, response assessment, therapy management, and drug/tracer development [8, 9].

Since the 1950s, there have been great advances with PET including the introduction of time-of-flight technologies [10], optimized detectors [11, 12], new radiotracers [13], iterative reconstruction algorithms [14, 15], and novel quantitative methods [16, 17] by a variety of scientists in physics, engineering, chemistry, mathematics, and statistics [18–20]. However, some constraints such as the limited axial coverage

Fengyun Gu and Qi Wu contributed equally to this work.

✉ Fengyun Gu
fengyungu@126.com

¹ School of Mathematics and Physics, North China Electric Power University, 102206 Beijing, China

² School of Mathematical Sciences, University College Cork, T12XF62 Cork, Ireland

still exist [21]. Currently, the conventional PET/CT systems have a short axial field of view (AFOV) of about 15 ~ 30 cm and typically only a specific organ such as the brain is imaged. On these scanners, whole-body (even dynamic) scanning can be performed by a multi-bed scenario, but pitfalls like the missing early-phase data and low temporal resolution limit its wide use [22].

The revolutionary total-body (TB) PET scanners (e.g., uEXPLORER [23], PennPET Explorer [24], and Siemens Biograph Vision Quadra [25]) have been developed to overcome these limitations. Such devices enable the simultaneous image of entire human body or main organs using a single-bed position. Given their ultra-high sensitivity (10~40 fold), extended field of view (1~2m), and enhanced temporal resolution (20~200 time frames), the potential clinical applications of these innovative technologies have been exploited in different ways to provide better image quality [25–28], reduce scan time [29–34], lower the injected dose [35–38], and develop new drugs; see [21, 39–44] for more descriptions. Next to all the exciting opportunities that arise with TB systems, there remain some challenges. The analysis of large-scale data, especially for dynamic scanning, becomes one.

Quantitation of dynamic PET studies could be able to provide additional biological information, and the potential benefits have been highlighted in precision medicine [45–47]. A broad family of quantitative techniques with focus on the recovery of arterial input function and the establishment of tracer kinetic model has been proposed to estimate the kinetic parameters of interest. The other procedures including motion correction and denoising also have some impacts on the estimated kinetics. Many different points of view have been taken in extensive literature and more comprehensive references [8, 16, 17, 48–52] are suggested for further readings. The aim of this review is to provide an overview of the basic principles and model formulations of the most important strategies for PET quantitation, along with their feasibilities and recent developments for the emerging total-body PET imaging. The future perspectives to further enhance quantitative accuracy are discussed as well.

Total-body PET studies

Since the first total-body human imaging was obtained on the uEXPLORER scanner in Zhongshan hospital [23], the spread of uEXPLORER with other long axial field of view (> 1m) systems has become worldwide. Up to 2022, more than 10 total-body PET/CT scanners, including uEXPLORER, PennPET Explorer, and Biograph Vision Quadra, have been installed in China [53], the USA [24, 54], and Europe [25, 38, 55]. The use of such scanners in both clinical (static mode) and research (dynamic mode) settings is emerging. Figure 1

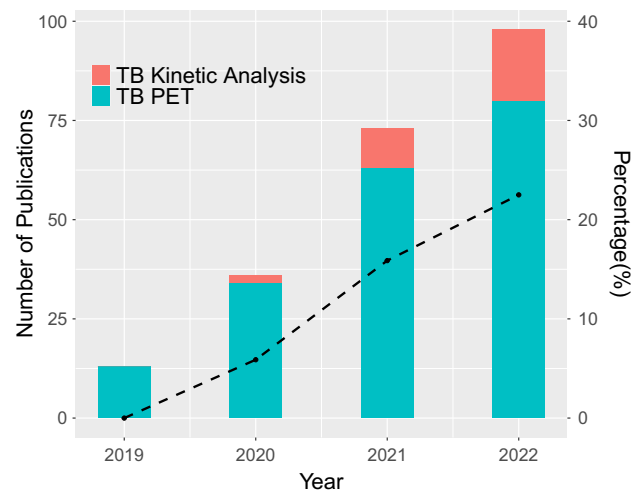


Fig. 1 The number of publications (left y-axis) on the total-body (TB) PET studies (blue) and dynamic TB scanning with the implementation of kinetic analysis (red) for the period from 2019 to 2022. The percentage (right y-axis) of publications relevant to the kinetic model in TB PET is shown as the black line. The data were collected from a search on PubMed on 08/05/2023

shows the trend for the work in the area of total-body PET from 2019 to 2022. The number of publications has a significant increase and reached to approximate 200 over the past 4 years. The proportion of dynamic studies with the implementation of kinetic analysis in total-body PET also steadily increases each year.

A list of reported dynamic total-body PET study cohorts along with the specific details is provided in Table 1. Several types of subjects were recruited: healthy volunteers and patients diagnosed with cancer or infected with COVID-19. While the most of scans were done exclusively with the administration of fluorine-18 labeled fluorodeoxyglucose (^{18}F -FDG), there are other radiotracers of interest to be employed, such as ^{68}Ga -FAPI-04 [56–58], ^{15}O -H $_2$ O [59], ^{89}Zr -Df-Cremirlimab [60, 61], ^{18}F -Fluciclovine [62], and [^{11}C]methionine [63]. A range of scanning and reconstruction protocols have been applied by different hospitals/institutions, but the magnitude of image voxels is generally on the order of ten million, and a more dense sequence is commonly performed at the early time. Although these dynamic datasets may not be consistent, the data analysis should face similar problems that will be discussed carefully in the next section.

Opportunities and challenges in dynamic total-body PET imaging

As summarized in Table 2, the unique characteristics of total-body PET studies bring a series of new challenges and

Table 1 List of reported dynamic studies on total-body PET scanners (uEXPLORER, PennPET Explorer, and Biograph Vision Quadra)

PET scanner	Radiotracer	No	(Voxels, time-frames)	Subject type	Site	Temporal sequences	Ref
uEXPLORER	^{18}F -FDG	1	(236 × 236 × 679, 187)	Healthy	[a]	60 × 1s, 30 × 2s, 20 × 3s, 12 × 10s, 50 × 30s, 15 × 120s	[64]
	^{18}F -FDG	11	(236 × 236 × 679, 97)	Healthy	[a]	24 × 5s, 73 × 60s	[29]
	^{18}F -FDG	30	(236 × 236 × 679, 60)	Healthy	[a]	36 × 5s, 24 × 180s	[35, 65, 66]
	^{18}F -FDG	35	(236 × 236 × 679, 55)	Cancer	[a]	36 × 5s, 19 × 180s	[67]
	^{68}Ga [Ga-DOTA-FAPI-04]	19	(192 × 192 × NA, NA)	Malignancy	[a]		[58]
	^{68}Ga [Ga-DOTA-TATE]	7	(192 × 192 × NA, 55)	Cancer	[a]	36 × 5s, 19 × 180s	[68]
	^{18}F -FDG	7	(192 × 192 × 672, 70)	Cancer	[b]	30 × 5s, 15 × 30s, 25 × 120s	[69]
	^{18}F -FDG	28	(192 × 192 × 672, 66)	Healthy/cancer	[b]	24 × 5s, 6 × 10s, 6 × 30s, 6 × 60s, 24 × 120s	[70]
	^{18}F -FDG	15	(192 × 192 × 673, 25)	Cancer	[b]	1 × 30s, 3 × 10s, 4 × 30s, 5 × 60s, 4 × 180s, 8 × 300s	[31]
	^{18}F -FDG	200	(192 × 192 × 673, 98)	Healthy/cancer	[b]	50 × 2s, 20 × 10s, 10 × 30s, 10 × 60s, 8 × 300s	[71]
	^{18}F -FDG	13	(150 × 150 × 486, 120)	Healthy	[c]	60 × 1s, 30 × 2s, 6 × 10s, 6 × 30s, 12 × 120s, 6 × 300s	[72]
	^{18}F -FDG	21	(150 × 150 × 486, 66)	Healthy/cancer	[c]	30 × 2s, 12 × 10s, 6 × 30s, 12 × 120s, 6 × 300s	[73]
	^{18}F -FDG	10	(150 × 150 × 486, 29)	Healthy/cancer	[d]	6 × 10s, 2 × 30s, 6 × 60s, 5 × 120s, 4 × 180s, 6 × 300s	[54]
	^{18}F -FDG	7	(NA, 120)	COVID-19	[d]	60 × 1s, 30 × 2s, 6 × 10s, 6 × 30s, 12 × 120s, 6 × 300s	[74]
	^{11}C -Butanol	3	(NA, 29)	Healthy/peripheral artery disease	[d]	12 × 5s, 6 × 10s, 6 × 30s, 5 × 300s	[75]
	^{89}Zr -Df-Cremirimab	8	(512 × 512 × NA, 46)	Healthy/COVID-19	[d]	6 × 60s, 16 × 30s, 2 × 60s, 12 × 120s, 10 × 300s	[60, 61]
	^{18}F -Fluciclovine	37	(256 × 256 × NA, NA)	Cancer	[d]		[62]
	^{18}F -FDG	30	(360 × 360 × 672, 92)	Cancer	[e]	30 × 2s, 12 × 5s, 6 × 10s, 4 × 30s, 25 × 60s, 15 × 120s	[76]
	^{68}Ga -FAPI-04	9	(239 × 239 × 679, 92)	Cancer	[f]	30 × 2s, 12 × 5s, 6 × 10s, 4 × 30s, 25 × 60s, 15 × 120s	[56]
	^{68}Ga -FAPI-04	13	(360 × 360 × NA, 92)	Cancer	[f]	30 × 2s, 12 × 5s, 6 × 10s, 4 × 30s, 25 × 60s, 15 × 120s	[57]
	^{11}C]methionine	12	(NA, 67)	Multiple myeloma (MM)	[f]	30 × 2s, 12 × 5s, 6 × 10s, 4 × 30s, 15 × 60s	[63]

Table 1 continued

PET scanner	Radiotracer	No	(Voxels, time-frames)	Subject type	Site	Temporal sequences	Ref
PennPET Explorer	¹⁸ F-FDG	4		Healthy/cancer	[g]		[24, 77]
Biograph Vision Quadra	¹⁸ F-FDG	12	(220 × 220 × 708, 31)	Cancer	[h]	6 × 10s, 3 × 20s, 6 × 30s, 5 × 60s, 11 × 300s	[55]
	¹⁸ F-FDG	24	(440 × 440 × 645, 62)	Cancer	[i]	2 × 10s, 30 × 2s, 4 × 10s, 8 × 30s, 4 × 60s, 5 × 120s, 9 × 300s	[25, 78, 79]
	[⁸² Rb]Cl	1		Atypical chest pain	[i]		[80]
	¹⁵ O-H ₂ O	5	(440 × 440 × 645, 54)	Cancer	[j]	1 × 5s, 30 × 1s, 15 × 2s, 5 × 10s, 3 × 20s	[59]

The corresponding radiotracer, the number of patients (No.), data dimension (voxels, time-frames), subject type, site of scanning and temporal sequences in each cohort are presented

- [a] Zhongshan Hospital, Fudan University, Shanghai, China
- [b] Henan Provincial People's Hospital, People's Hospital of Zhengzhou University, Henan, China
- [c] University of California Davis, California, USA
- [d] University of California Davis EXPLORER Molecular Imaging Center, California, USA
- [e] Sun Yat-Sen University Cancer Center, Guangzhou, China
- [f] Renji Hospital, Shanghai, China
- [g] University of Pennsylvania, Philadelphia, USA
- [h] University of Groningen, Groningen, The Netherlands
- [i] Bern University Hospital, University of Bern, Bern, Switzerland
- [j] University of Copenhagen, Denmark

Table 2 Characteristics and challenges/opportunities of total-body PET scanners

Characteristics	Challenges/opportunities
Multiple organs/tissues	<ul style="list-style-type: none"> • Tissue-specific kinetics • Large blood pool in FOV • Heterogeneity • Delay correction
Higher temporal resolution	<ul style="list-style-type: none"> • Capture fast kinetics
Higher spatial resolution	<ul style="list-style-type: none"> • Better image quality
Huge data set	<ul style="list-style-type: none"> • High computational cost

opportunities for improved quantitative accuracy. Details are presented below:

- (i) Improved image-derived input function: Due to the long axial field of view of total-body PET scanners, image-derived input functions can be measured from multiple blood pools (e.g., heart ventricle, aorta, and artery). Higher temporal resolution (e.g., 1 s even 0.1 s per early frame) also allows better temporal sampling of the extracted input function [43, 64, 81].
- (ii) Organ-dependent time delay: The arrival time of tracer to different organs is significantly varied, which has been an important factor for accurate total-body kinetics [54, 82–84].
- (iii) Tissue-specific kinetics: Each kind of tissue has its own physiological mechanism and some tissues such as the liver, kidney, and bladder even exhibit more complex kinetics. Thus, a single kinetic model may not be feasible for multiple organs, and appropriate model selection is necessary [54, 84–86].
- (iv) Capture fast kinetics: The high temporal sampling imaging provides an opportunity for better investigation of fast kinetics such as the blood volume or blood flow (perfusion), which are potential biomarkers for the prediction of therapy response or survival [87–90].
- (v) High-quality dynamic PET images: The increased sensitivity enables the generation of high signal-to-noise (SNR) images, which is greatly beneficial to the quantitation of dynamic imaging at the voxel level, e.g., noise reduction and lesion enhancement. But we need to note the sensitivity along the axial field of view shows the reciprocal U shape (non-uniform) [28, 91, 92]. Thus, images have higher variances towards the axial edge, which needs to be considered carefully.
- (vi) Huge data set: It is challenging to store and process such enormous and complex datasets, which may be addressed by some automation forms using more comprehensive approaches (e.g., segmentation) [93–98] or artificial intelligence [40, 85, 99–101]

Overview of dynamic PET quantitation

Dynamic PET quantitation is not a single procedure and involves several steps such as the recovery of input function and application of tracer kinetic modeling. The overview of this process is presented in Fig. 2. In the following sections, we will introduce the basic principles and some well-established methodologies, also their further developments for the emerging total-body PET imaging [43, 64, 78].

Basic equation

Understanding the targeted biochemical pathway is critical for the interpretation of dynamic PET imaging data. It can be approached using the indicator-dilution method built on the seminal work of Meier and Zierler [102]. Assuming the radiotracer's interaction with tissue is substantially linear and time-invariant (LTI), the vascular network can be regarded as an LTI system with an arterial input. Hence, the measured tissue time activity curve (TAC) - C_T can be expressed as a convolution between the arterial input function (C_p) and tissue residue, also called the impulse response function (R) as in Eq. 1.

$$C_T(t) = \int_0^t R(t-s)C_p(s)ds \equiv R(t) \otimes C_p(t) \quad (1)$$

With the known input function, kinetic analysis is concerned with the estimation of residue and associated kinetic parameters such as flow (K), flux (K_i) and volume of distribution (V_D).

$$K = R(0), \quad K_i = \lim_{t \rightarrow \infty} R(t), \quad V_D = \int_0^{\infty} R(t) dt \quad (2)$$

When the model is applied to PET time-course data, there is typically an adjustment for a biologically important parameter—blood volume (V_B). Moreover, the site to recover the input function may be remote from the tissue, introducing a time delay. The correction is generally accomplished by the inclusion of a delay term (Δ) in the modeling procedure as Eq. 3. The delay has been found to vary with different voxels/organs/tissues and its correction is necessary [54, 82–84].

$$C_T(t) = V_B C_p(t-\Delta) + (1-V_B) \int_0^t R(t-s)C_p(s-\Delta)ds \quad (3)$$

Some specific organs (e.g., liver) receive dual blood supplies from the hepatic aorta and portal vein [103–106]. To account for such an effect, the input function can be expressed

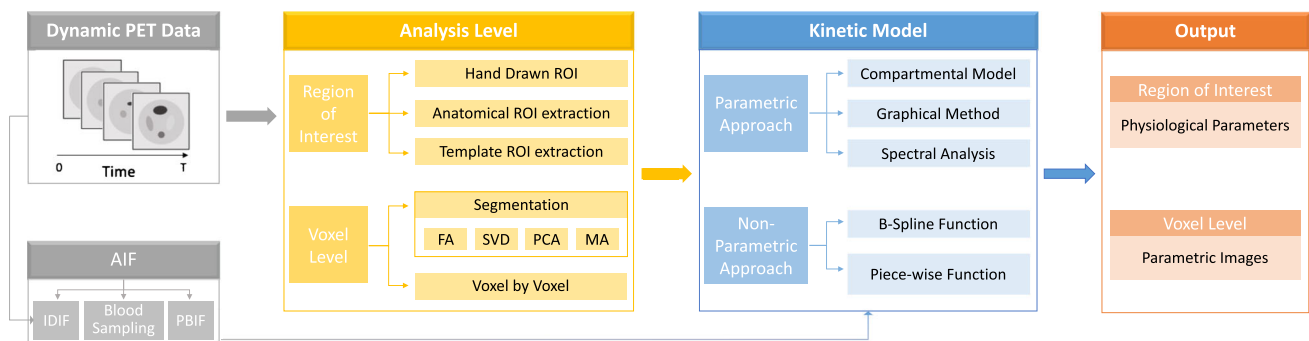


Fig. 2 Overview of dynamic PET quantitation. Abbreviations: PET, positron emission tomography; IDIF, image-derived input function; PBIF, population-based input function; ROI, region of interest; FA, factor analysis; SVD, singular value decomposition; PCA, principal component analysis; MA, mixture analysis

as a weighted sum of both supplies [107–109].

$$C_p(t) = (1 - f_A)C_{PV}(t) + f_A C_A(t) \quad (4)$$

where C_{PV} is the portal vein input and $C_A(t)$ is the aortic input. f_A is the fraction of hepatic artery to the overall liver blood flow.

Region of interest versus voxel-level analysis

The computation of kinetic parameters can be performed either at the regional or voxel level. Due to the average of the voxel information in a region of interest (ROI), the noise can be reduced dramatically. ROI analysis leads to more robust results, especially in the case of dynamic PET studies, but also introduces some biases when defining ROIs from a template, summed, or anatomic images [49]. An alternate approach to regional estimates is performing analysis at the voxel level and generated parametric images can reveal the heterogeneity of tumors [16]. However, many issues need to be considered carefully such as computational efficiency, selection of appropriate models, and noise suppression [54].

Total-body PET scanners have the ability to image more organs/tissues using the single-bed position, but the datasets are much bigger and complex than conventional studies. Multivariate statistical methods including factor analysis (FA) [95], singular value decomposition (SVD) [98], principal component analysis (PCA) [94, 97], and mixture analysis (MA) [93] express the dynamic PET data as a weighted sum of image volumes. They enable to identify organs and structures with different kinetic patterns in a temporal sequence and reduce the temporal and spatial variations of the noise [110]. Once the segmentation process is completed, kinetics for each segment TAC (sub-TAC) are calculated and then mapped back to the original spatial space. These data-driven

approaches have the great potential to efficiently handle the complexities and address variable noise issues in dynamic total-body images [96].

Arterial input function

For standard PET quantitation, the knowledge of the tracer arterial plasma concentration is required as an arterial input function (AIF). The input function can be derived either from (i) arterial blood samples, (ii) the time course of an ROI drawn on the PET image, or (iii) based on the population. Here, we provide a brief introduction to these commonly used and model-based approaches together with their applications in total-body PET studies. For more details, readers are referred to two recent review papers [111, 112].

Blood sampling

Arterial blood sampling during dynamic acquisition has been considered the standard for input function in many references [113–116]. But some concerns are also raised, for example, the measured AIF may suffer from some effects (e.g., delay, dispersion, and metabolites), which need to be corrected [112]. This invasive procedure also implies discomfort for the patient (insertion of arterial lines and increased radiation) and additional costs for the analysis of numerous blood samples. Thus, it is typically used for research purposes and not recommended for routine clinical practice.

Manual blood sampling or an automatic blood sampling system (ABSS) [117] is generally used to collect arterial blood. However, manual separation of plasma requires decay correction [118, 119], while longer tubing in ABSS introduces higher dispersion effects [120] and requires consideration of the blood-to-plasma ratio [121, 122]. Another issue

with AIF refers to the metabolite analysis. Although there do not exist blood-based metabolites for some tracers such as ^{18}F -FDG and ^{15}O - H_2O , most tracers produce isotope-labeled metabolites that contaminate the input function. These metabolites can be corrected by some mathematical models, e.g., hill model [123, 124], power model [125, 126], and exponential models [127]. A review of the commonly used metabolite-correction approaches is suggested to read for further details [128].

In practice, it would be more difficult to get the blood sampling for the total-body PET study. For example, both the radial artery and antecubital vein are harder to access due to the long axial field of view [40]. The long line from the wrist to the sampling site also may cause more serious delay and dispersion issues [112]. With so many challenges, the first attempt was made by a Denmark group to get the arterial blood sample for the total-body ^{15}O - H_2O scanning with Quadra [59]. Such clinical trials are expected to be conducted more in the future. On the other hand, some non-invasive techniques (based on image/population/mathematical models) have also been developed as follows.

Image-derived input function

To obviate the need for blood sampling, input information can be also derived from a region drawn at the blood pool on PET images, referred to as image-derived input function (IDIF). Due to the limited field of view of conventional PET scanners, sometimes IDIF can only be measured from small vessels such as carotids. However, total-body PET imaging provides multiple choices encompassing the left ventricle, aorta, and other big blood vessels [43, 64, 78]. So far, the IDIF recovered from an ROI over descending aorta (DA) has been the most popular one [17]. Furthermore, the high spatial and temporal resolutions may also lead to more accurate and less noisy IDIF.

However, the use of IDIF still needs to be investigated carefully in the total-body setting. The whole blood activity concentration can be derived, and plasma concentration is impossible to obtain. Reliable results are only generated with radiotracers that do not produce any metabolites, such as ^{18}F -FDG [49]. Additional corrections to the IDIF are also important for accurate kinetics [72].

Population-based input function

Assuming individuals have the same tracer injection protocol and similar physiological characteristics in a cohort, the population-based input function is generally calculated by averaging and scaling this set of input functions using arterial catheterization invasively [129]. Such a method is probably the most interesting approach for use in clinical practice with many radiotracers, but currently, it has been val-

idated almost exclusively for ^{18}F -FDG [130]. Several groups have attempted to reduce the dynamic scanning time using the PBIF on the total-body PET scanners [32, 55, 79].

Model-based input function

Model-based descriptions of the arterial samples are usually introduced to obtain continuous and noise-free input functions, which may be helpful to further improve IDIF or PBIF. The most famous models are Feng's model [131] and its variation, i.e., tri-exponential model [132], but they both cannot describe the complex behavior of the AIF and account for different injection protocols properly [133]. Simultaneous estimation of the input function (SIME) is usually used to generate a specific input function by fitting regional TACs simultaneously [134–136]. Recently, a population-based projection model (PBPM) has been developed which combines population profiling (as in a PBIF approach) with individual arterial input data modeling (as in an IDIF approach). This model incorporates knowledge of injection duration into the fit, allowing for varying injection protocols [137]. Another promising model to be applied to the emerging total-body PET imaging is the novel Markov chain model for the representation of the whole-body tracer circulation [138].

Kinetic model

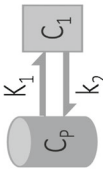
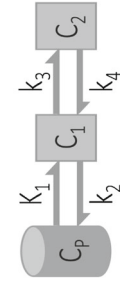
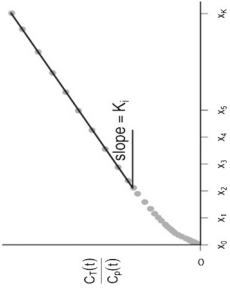
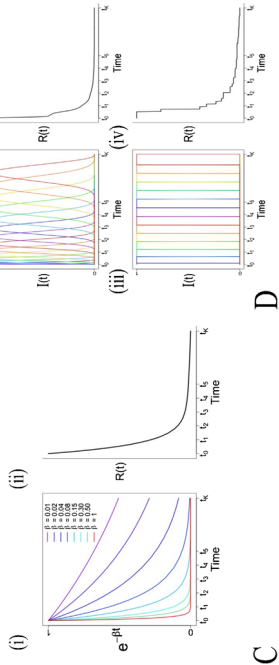
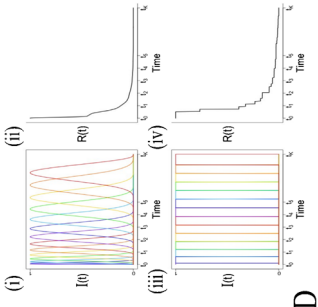
Many kinetic models have been well-developed for quantitative PET scanning, but they differ in terms of residue form and produced information [49]. A summary is shown in Table 3. Most of them (e.g., compartmental model, Patlak plot, and spectral analysis) is a parametric model that generally relies on the necessary assumptions. These are difficult to justify for the heterogeneous tissue region, especially the diverse-tissue study. The non-parametric method without the assumption requirement should be more flexible and indeed have some substantial advantages.

Here, we provide an overview of various parametric and nonparametric strategies (see [88] for more details of derivations) and summarize their recent developments for total-body PET imaging [54, 64, 73, 78, 83, 84, 86, 139, 140]. The feasibility, challenge, and promise of these methodologies are also discussed.

Compartmental model

Compartmental modeling forms the basis for tracer kinetics of dynamic PET data. There are two most important models used to derive physiological information in absolute measurement units as shown in Table 3 (A). One tissue compartmental (1C) model with two rate constants (K_1 in

Table 3 A summary of major kinetic models used in PET quantitation

Kinetic model	Compartmental model	Patlak plot	Spectral analysis	Non-parametric analysis
Graphical representation				
	<p>1C: </p> <p>2C: </p>	<p></p> <p>A</p>	<p></p> <p>C</p>	<p></p> <p>D</p>
Formula	<p>1C: $\frac{dC_1(t)}{dt} = K_1 C_p(t) - k_2 C_1(t)$</p> <p>2C: $\frac{dC_1}{dt} = K_1 C_p(t) - (k_2 + k_3) C_1(t) + k_4 C_2(t)$</p> <p>2C: $\frac{dC_2}{dt} = k_3 C_1(t) - k_4 C_2(t)$</p>	<p>$\frac{C_T(t)}{C_p(t)} = K_i \frac{\int_0^t C_p(\tau) d\tau}{C_p(t)} + C, t \geq t^*$</p>	<p>$C_T(t) = \sum_{j=0}^J \alpha_j g_j(t), \alpha_j \geq 0$</p> <p>$C_T(t) = \sum_{j=0}^J \alpha_j f_j(t), \alpha_j \geq 0$</p>	
Residue form	<p>1C: $R(t) = K_1 e^{-k_2 t}$</p> <p>2C: $R(t) = K_1 (\pi_1 e^{-\theta_1 t} + \pi_2 e^{-\theta_2 t})$</p>	<p>$R(t) = K_i, t \geq t^*$</p>	<p>$R(t) = \sum_{j=0}^J \alpha_j e^{-\beta_j t}$</p> <p>$R(t) = \sum_{j=1}^J \alpha_j I_j(t)$</p>	
Kinetic parameters	All	Only K_i	All	All
Computation	Nonlinear least square or maximum likelihood	Ordinary least square	Non-negative least square	Quadratic programming
Application to TB PET	Yes	Yes	No	Yes
References	[54, 57, 60, 63, 66, 68, 70, 72, 78, 82–84]	[31, 32, 43, 55, 57, 64, 70, 78, 86, 139]		[140]

*For details of derivations, see [88]

A: One (1C) and two compartmental (2C) models. C_p is the plasma compartment; C_1 and C_2 are tissue compartments

B: Patlak plot

C: Spectral analysis. (i) exponential distribution for different values of β ; (ii) the typical residue estimated by spectral analysis

D: Non-parametric analysis. (i) general form of B-spline basis elements; (ii) the typical residue estimated by B-spline function;

(iii) general form of piece-wise elements; (iv) the typical residue estimated by piece-wise function

$$\begin{cases}
 \pi_1 = \frac{k_4 - \theta_1 + k_3}{\theta_2 - \theta_1}, \pi_2 = \frac{\theta_2 - k_4 - k_3}{\theta_2 - \theta_1} \\
 \theta_1 = \frac{k_2 + k_3 + k_4 - \sqrt{(k_2 + k_3 + k_4)^2 - 4k_2 k_4}}{2} & g_j(t) = C_p(t) \otimes e^{-\beta_j t} & f_j(t) = C_p(t) \otimes I_j(t), I \text{ represents basis function (B-spline or piece-wise form)} \\
 \theta_2 = \frac{k_2 + k_3 + k_4 + \sqrt{(k_2 + k_3 + k_4)^2 - 4k_2 k_4}}{2}
 \end{cases}$$

ml/min/cm³ and k_2 in min⁻¹) was developed by Kety [141] for quantitative assessment of blood flow (perfusion). Two tissue reversible compartmental (2Cr) model with four rate constants (K_1 in ml/min/cm³, k_2 , k_3 and k_4 in min⁻¹) is mainly used for quantifying receptor-ligand binding studies [142]. While k_4 equals 0 (irreversible), it becomes the most famous Sokolov-Huang model (2Ci) generally employed for the quantitation of metabolic rate for glucose [143–145]. For more generalized compartmental models and detailed underlying biochemical mechanisms, see [48].

These models are described by a system of first-order time-dependent differential equations, which can be solved by a numerical procedure known as nonlinear least squares (NLS) in order to appropriately estimate the residue function and associated kinetics. The advantages of compartmental modeling are the reliability and independency on the scanning time. When dealing with very noisy data (e.g., voxel-level analysis), this method has several shortcomings including convergence issues, long computational time, and sensitivity to initial estimates due to the nature of NLS [49].

1C model

One tissue compartmental model is given by a differential equation as Eq. 5:

$$\frac{dC_1(t)}{dt} = K_1 C_p(t) - k_2 C_1(t) \tag{5}$$

where C_1 represents tissue compartment and C_p is the plasma compartment. Solved by the integrating factor method, the solution is found to be as follows:

$$C_1(t) = \int_0^t K_1 e^{-k_2(t-s)} C_p(s) ds \tag{6}$$

Related to the simple basic Eq. 1, the residue function can be expressed as

$$R(t) = K_1 e^{-k_2 t} \tag{7}$$

Hence, the parameter of interest - blood flow (perfusion) = $R(0) = K_1$.

2C model

Similar to the 1C model, two tissue compartmental model is represented by a coupled system of differential equations as

Eq. 8.

$$\begin{cases} \frac{dC_1}{dt} = K_1 C_p(t) - (k_2 + k_3) C_1(t) + k_4 C_2(t) \\ \frac{dC_2}{dt} = k_3 C_1(t) - k_4 C_2(t) \end{cases} \tag{8}$$

where C_2 is the tissue compartment. By the Laplace transform and its inversion [146], the final result is given by the following:

$$C_T(t) = C_1(t) + C_2(t) = K_1 (\pi_1 e^{-\theta_1 t} + \pi_2 e^{-\theta_2 t}) \otimes C_p(t) \tag{9}$$

where

$$\begin{cases} \pi_1 = \frac{k_4 - \theta_1 + k_3}{\theta_2 - \theta_1}, \pi_2 = \frac{\theta_2 - k_4 - k_3}{\theta_2 - \theta_1} \\ \theta_1 = \frac{k_2 + k_3 + k_4 - \sqrt{(k_2 + k_3 + k_4)^2 - 4k_2 k_4}}{2} \\ \theta_2 = \frac{k_2 + k_3 + k_4 + \sqrt{(k_2 + k_3 + k_4)^2 - 4k_2 k_4}}{2} \end{cases}$$

Again recall the fundamental Eq. 1, residue is a mixture of exponentials as Eq. 10.

$$R(t) = K_1 (\pi_1 e^{-\theta_1 t} + \pi_2 e^{-\theta_2 t}) \tag{10}$$

For the irreversible 2C model ($k_4 = 0$), the metabolic flux is focused, that is $K_i = \lim_{t \rightarrow \infty} R(t) = \frac{K_1 k_3}{k_2 + k_3}$. For the reversible tracers, volume of distribution is calculated as: $V_D = \int_0^\infty R(t) dt = \frac{K_1}{k_2} (1 + \frac{k_3}{k_4})$.

Delay effect

In the routine PET image, IDIF is usually extracted from a nearby arterial blood pool, so the time delay between IDIF and the targeted tissue is very short and even negligible. The total-body PET scanner provides several options for IDIF location that may be far away from some tissues. The delay time can be up to 50s and significantly varied to different tissues, which has been an important factor to affect the kinetic quantification [54, 82–84].

To correct this effect, the delay term is jointly estimated with other parameters in compartmental models. Take 1C model as an example, replacing the residue function in Eq. 3 by Eq. 7 gives:

$$C_T(t) = V_B C_p(t - \Delta) + (1 - V_B) \int_0^t K_1 e^{-k_2(t-s)} C_p(s - \Delta) ds \tag{11}$$

In this setting, (V_B, K_1, k_2, Δ) are estimated. Similarly for 2C model, ($V_B, K_1, k_2, k_3, \Delta$) or ($V_B, K_1, k_2, k_3, k_4, \Delta$)

are derived, but the estimation procedure is more computationally expensive. Two schemes have been proposed to determine the delay by only the first few minutes data using 1C model [82, 83] or full-time data in arbitrary models [54]. The former one has been initially demonstrated to be efficient [84].

Model selection

The selection of compartmental models (1C, 2Ci, 2Cr) usually depends on the tracer property, the aim of study, and even the organ or tissue of interest. For example, 1C is generally adopted for $^{15}\text{O}\text{-H}_2\text{O}$ and 2Cr is used for $^{11}\text{C}\text{-Raclopride}$. As the most commonly used tracer - $^{18}\text{F}\text{-FDG}$, the irreversible model (2Ci) is employed for many organs while its uptake into the liver exhibits reversible characteristics [147]. Therefore, we must justify each case carefully for the use of compartmental model.

The typical quantitation for dynamic PET study is applying a single model, which works well in organ-specific imaging on conventional scanners. But it may not be appropriate for total-body imaging as a single model is hard to be feasible for diverse tissues and organs. Wang et al. have reported that voxel-level model selection strategy based on an Akaike information criterion (AIC) leads to improved total-body parametric imaging [54]. But there is no doubt that it brings more computation burden. Later on, a further examination of various compartmental models for multiple organs is implemented at the ROI level [84]. This study indicates that the applicability of compartmental models for the bladder is questionable.

Patlak plot

Graphical techniques provide simple ways to estimate the specific kinetic parameters by appropriately transforming the equations of compartmental modeling for irreversible and reversible tracers [148–150]. Here, we just focus on the most popular graphical method—Patlak model; for more details about other approaches, we suggest a review article for further reading [151]. Patlak analysis has been widely applied to dynamic PET imaging due to its simplicity and robustness [148], which is assumed that (i) the trapping of tracer in studied organs/tissues is completely irreversible; (ii) Patlak plot results in a straight line after the time that steady-state conditions between reversible tissue and plasma compartments are reached. If both assumptions are satisfied, K_i can be estimated easily as the slope of Patlak plot after the equilibrium time (t^*) using linear regression. The Patlak plot is given by

the expression below:

$$\frac{C_T(t)}{C_P(t)} = K_i \frac{\int_0^t C_P(\tau) d\tau}{C_P(t)} + \text{constant}, \quad t \geq t^* \quad (12)$$

K_i is computed using a few late time frames of dynamic scanning by a non-iterative strategy—ordinary least square (OLS). Due to the nature of linearity, it should be much faster and less sensitive to noise than NLS, and it is therefore appropriate for applications at the voxel level [8]. On the other hand, it must be noted that this approach does not provide any insight regarding the complete profile of tracer kinetics and only a reduced set of parameters (K_i) is obtained.

When adopting the standard Patlak (sPatlak) method for dynamic total-body imaging, many tissues and organs can be studied simultaneously. Single t^* may not be appropriate for the diverse-tissue environment as the equilibrium conditions probably achieve at different time points. The feasibility of Patlak plot also needs to be justified for certain tissues like the liver, kidney, and bladder. These limitations and possible solutions are discussed in detail in the following.

Selection of t^*

The improper t^* may introduce additional errors in estimated K_i [152]. A rich literature has explored the choice of t^* for single organ on short AFOV PET scanners, for example, 20 min for brain [153] and 10 min for lung [154]. Total-body Patlak images are generated with various t^* , from 10 min [155], 15 min [29], 20 min [156] to 30 min [64]. But there are no more details about the justifications in these studies.

Recently, an adaptive t^* scheme has been proposed to determine the optimal options for different ROIs or voxels [139]. It is based on two criteria: max-error and R squared (R^2). Max-error is defined as the worst case error between the predicted value and the true value for all observations on Patlak plot. The selected t^* is the earliest one so that max-error is less than a threshold value. This criterion has been employed in PMOD (Zürich, Switzerland), and the default setting of threshold is 10%. R^2 is a common metric to quantify the goodness of linear fit, and a value closer to 1 indicates a better fit, so optimal t^* is determined by the maximum R^2 . This procedure has the potential to improve the accuracy of kinetic parameters. However, further investigations in patient cohorts and more sophisticated techniques need to be developed.

Generalized patlak

As described above, the standard Patlak analysis assumes an irreversible 2C model. For total-body imaging, this assump-

tion can be broken by some tissues (e.g., the liver where ^{18}F -FDG may exhibit mild positive uptake reversibility and bladder associated with the complex tracer excretion process) [84, 139, 157] and tumors (e.g., hepatocellular carcinoma) [158] so that the sPatlak plot is no longer linear.

To address these issues, a generalized Patlak (gPatlak) method Eq. 13 based on the reversible 2C model was proposed in 1985 [159], which introduced an additional exponential term characterized by the net efflux (k_{loss}) to account for the effect of tracer dephosphorylation properly.

$$\frac{C_T(t)}{C_p(t)} = K_i \frac{\int_0^t e^{-k_{loss}(t-\tau)} C_p(\tau) d\tau}{C_p(t)} + \text{constant}, t \geq t^* \quad (13)$$

This model becomes non-linear due to the added exponential term, but it can be solved by applying a basis function to linearize the estimation process [160].

The utility of gPatlak approach for diverse organs and tissues is first examined by Karakatsanis et al. [160] in multi-bed multi-pass whole-body PET imaging. Then, the performance of both standard and generalized Patlak methods has been assessed for multiple organs at the ROI level using a total-body PET study on uEXPLORER [86]. Results show that gPatlak can bring benefits for the liver, kidney, lung, and especially bladder. Thus, it would be also interesting to explore the use of gPatlak plot for voxel-level analysis in the future.

Spectral analysis

The residue function in the compartmental model is the single exponential Eq. 7 or a mixture of exponentials Eq. 10. It may not have sufficient degrees of freedom to capture full variability in total-body PET data. Spectral analysis (SA) proposed by Cunningham and Jones in 1993 [161] assumes the residue to be the sum of $J + 1$ exponential terms.

$$R(t) = \sum_{j=0}^J \alpha_j e^{-\beta_j t}, \alpha_j \geq 0, \beta_j \geq 0, \beta_0 = 0 \quad (14)$$

Thus, the tissue time course can be expressed as

$$C_T(t) = \sum_{j=0}^J \alpha_j e^{-\beta_j t} \otimes C_p(t) \equiv \sum_{j=0}^J \alpha_j g_j(t) \quad (15)$$

$g_j(t)$ are known with the pre-defined eigenvalues β_j , whereas the amplitudes α_j are estimated by the NLS algorithm. The model structure (e.g., reversibility or irreversibility, number of compartments) is derived from α_j , also called spectrum

[8]. The information of macroparameters, such as K , K_i , and V_D is obtained as follows:

$$K = \sum_{j=0}^J \alpha_j, \quad K_i = \alpha_0, \quad V_D = \sum_{j=1}^J \frac{\alpha_j}{\beta_j} \quad (16)$$

Some relevant strategies such as rank-shaping spectral analysis [162] and spectral analysis with iterative filter [163] have also been developed in recent years. The main strength of spectral analysis is its flexibility which can be applied to reversible or irreversible tracers, single or multiple compartmental models, and homogeneous as well as heterogeneous systems [50]. These characteristics make this method adaptable to various tracers and particularly suitable for total-body PET imaging. But until now, it has not been implemented in this area.

Non-parametric analysis

Typically, the tissue residue is a monotone decreasing function and approximated as nonnegative sums of exponential terms in the compartmental framework. However, the strict monotonicity ($\Delta R(t) < 0$) is not always realistic [164] and the assumed exponential form may not be reasonable to represent data in which in vivo biochemistry is not clear [165–168], especially for the emerging total-body PET imaging [84, 86].

Unlike the methods discussed above, residue can be also estimated by the non-parametric approaches [169–172] and given by the following:

$$R(t) = \sum_{j=1}^J \alpha_j I_j(t), \quad \alpha_j \geq 0 \quad (17)$$

Although it has a similar structure as Eq. 14, I here represents the basis elements, which can be B-spline [169, 172] or piece-wise function [170, 171]. This procedure has the ability to adapt to monotone (even exponential) and non-monotone forms as no unrealistic parametric restrictions are imposed.

The non-parametric residue analysis can be implemented rapidly by quadratic programming and has the advantage to provide more accurate kinetic quantitation in multiple tissues. An efficient application of this concept to generate parametric imaging is described as follows.

Non-parametric residue mapping

The non-parametric residue mapping (NPRM) consists of a fully automatic process incorporating data-adaptive segmentation, non-parametric residue analysis of segment data (sub-TAC), and voxel-level kinetic mapping scheme [173].

Following the linear structure of mixture model [93], the voxel-level time course (z_i) can be expressed as a non-negative combination of sub-TACs (μ_l). The mechanism enables to address the heterogeneity of voxel-level data.

$$z_i(t) = \sum_{l=1}^L \pi_{il} \mu_l(t), \quad \pi_{il} \geq 0, \quad i = 1, 2, \dots, N \quad (18)$$

where π is the coefficient and N is the number of voxels.

For each sub-TAC, the associated residue is estimated non-parametrically, and the parameter of interest - θ (e.g., K , K_i or V_D) can be derived as a function (g) of residue.

$$\mu_l(t) = R_l(t) \otimes C_p(t - \Delta) \Rightarrow \theta_l = g(R_l)$$

The final parametric imaging is obtained as

$$\theta_i = \sum_{l=1}^L \pi_{il} \theta_l, \quad i = 1, 2, \dots, N \quad (19)$$

The NPRM approach has some important features like the flexibility for diverse tissues and consideration of delays for different parts and also the ability to address issues with bladder or injection site [169, 171, 173], which make it feasible to be applied to total-body PET studies.

Building on Eq. 18, an image-domain bootstrap data generation process can be defined by the spatial and temporal patterns of model residuals [174, 175]. It has been used to assess the uncertainty (standard errors) of parametric imaging [176]. The practicality of simultaneous segmentation, kinetic parameter estimation, and uncertainty evaluation has also been demonstrated for a total-body breast cancer patient study on Biograph Vision Quadra [140].

Other approaches

All the aforementioned approaches are applied in the image domain; however, they can be incorporated into the reconstruction process to estimate kinetic parameters by modeling projection data (sinogram or list-mode), known as the “direct method” [177]. The ideas for direct estimation could date back to the 1980s [178, 179], and since then, many scientists made great contributions to the progression of this technology for more accurate kinetics than the routine post-reconstruction procedure [180–185]. We suggest a detailed technical review for further reading [186]. It is remarkable that direct Patlak has been adopted on commercial scanners and applied to total-body PET studies [64, 78, 187]. But it suffers from similar problems like the non-linearity for specific tissues as mentioned above [86, 139, 188].

Another research interest in future work is the implementation of artificial intelligence (AI) for the total-body PET imaging [99, 189]. As a subcategory of AI, deep learning (DL) techniques, e.g., convolutional neural network (CNN) [190] and generative adversarial network (GAN) [101], have been extensively used in PET for solving a wide variety of problems involving image reconstruction [191–193], denoising [194, 195], segmentation [196, 197], and quantitation [198, 199]. A few initial attempts have been made to extract the flux (K_i) from total-body PET studies by DL methods [71, 187, 200]. More opportunities and challenges facing the adoption of DL in total-body PET quantitation are detailedly discussed in a recent review paper [85].

There are a number of PET studies where dynamic scans are used and main organs are included, e.g., whole-body human and preclinical animal imaging. The data structures and characteristics are similar to total-body human studies. Therefore, it is natural to generalize the techniques developed in these studies for quantifying dynamic total-body imaging. For example, (i) generalized and direct Patlak methods are both first examined for multiple organs in whole-body scans [160, 201, 202], then applied to total-body imaging [64, 78, 86]; (ii) the above-mentioned NPRM procedure is demonstrated in the whole-body pregnant macaque studies [203] before it is employed to generate total-body parametric imaging [140]. Many other perspectives also have excellent potential as tools in the future [22, 204].

Discussion

Outside of the quantitative procedures discussed in this review, there are some basic challenges (e.g., motion, spillover, and partial volume) in the pre-processing strategy that may limit the reliability of estimated kinetics. Patient movement, respiration motion, and cardiac motion are unavoidable during the PET acquisition, particularly for the dynamic scanning with longer time. Many methods to correct motion have been proposed, and most of them are based on image registration algorithms or hardware motion tracking using an external device [49]. To the best of our knowledge, there is no common approach to resolve this issue for all organs even if it is well studied in the brain images. But we are glad to see that it has been investigated in the total-body studies by some researchers [205]. Another measure, denoising, is sometimes taken to ensure accurate results. Typically, one selected filter, e.g., Gaussian or non-local mean, is applied to reduce the PET image noise before the formal quantitation [206]. For a more comprehensive discussion on pre-processing procedures, we refer the reader to a recent article [87].

Although the emergence of total-body PET scanners brings a series of benefits, the concerns of the adoption of

dynamic studies in clinical practice still remain, even more serious. For example, more static scans can be completed in a specific time interval (e.g., 1 h) as they can be acquired faster on uEXPLORER [30]. It may be argued that the cost of dynamic studies would be substantially higher. Thus, some protocol designs, e.g., dual-injection scheme [69], have been explored to reduce the dynamic scanning time. At the same time, parameter estimation procedures including non-invasive input functions and improved kinetic models are developed to make dynamic imaging more feasible and valuable in routine use [177]. Regardless of these difficulties, the additional information recovered from dynamic PET scans has been demonstrated to be useful to predict therapy response or survival [89, 90], which deserves to be appreciated in precision medicine for improving individualized treatment by maximizing the therapeutic effect and minimizing toxicity [46]. From all these perspectives, the role of dynamic PET imaging may not be changed in the short run, but we are confident that it must have a bright future in clinics.

During the past few years, many groups (>20) in nuclear medicine, physics, biomedical engineering, and statistics have been involved in the total-body PET data acquisition and analysis. The early adopters have generously shared their insights into this new technology. Hicks provided an installation guide including many aspects (e.g., financing, space, and power) for total-body PET/CT beginners [207]. Vandenberghe et al. proposed a few design options to reduce the cost for total-body PET [208]. Bern group shared their experience obtained from 7000 patient studies on Quadra [209]. An expert consensus was also proposed for the oncological use of uEXPLORER with ^{18}F -FDG based on the experience of imaging 40,000 cases [210]. These reports greatly improve our understanding of the clinical use of advanced total-body systems. However, until now, there is no standardized framework for data structure, storage, sharing, and reproducibility, which may be similar to the Brain Imaging Data Structure (BIDS) platform promoted by the brain imaging community [211, 212]. The construction of such a platform needs the collaboration of multiple teams in diverse disciplines, but it is a worthwhile endeavor to release the full potential and pave the way for further developments of total-body PET scanners.

Conclusions

In the coming years, total-body PET technologies are expected to have a more widespread impact. The review of basic principles and recent advances in general quantitation strategies may facilitate their use and validation in total-body imaging and subsequently enhance the reliability of derived kinetic information. The promise of some novel approaches (either deep learning or multivariate statistical methods) to

improve quantitative accuracy is also pointed out. Overall, there is still a long way to fully understand and handle the complexities of total-body dynamics.

Acknowledgements F. Gu and Q. Wu acknowledge Prof. Finbarr O'Sullivan at University College Cork (UCC) for introducing them to quantitative analysis of dynamic PET imaging and delivering many pioneering and insightful ideas. The authors would like to thank Prof. Kuangyu Shi and Prof. Axel Rominger at Bern University Hospital who generously share the latest data on Biograph Vision Quadra with UCC Biomedical Imaging team, so that they have the experience to deal with long axial field of view PET studies. They would also like to thank Prof. Yun Zhou for providing them with opportunities to do research on uEXPLORER Total-Body PET studies in Central Research Institute, United Imaging Healthcare from August/September to December 2021. The insightful comments of anonymous reviewers also greatly improved this work.

Funding This work was supported by the Fundamental Research Funds for the Central Universities (2023MS077). Open Access funding provided by the IReL Consortium

Declarations

Ethical approval This article does not contain any studies with human participants or animals performed by any of the authors.

Conflict of interest The authors declare no competing interests.

Open Access This article is licensed under a Creative Commons Attribution 4.0 International License, which permits use, sharing, adaptation, distribution and reproduction in any medium or format, as long as you give appropriate credit to the original author(s) and the source, provide a link to the Creative Commons licence, and indicate if changes were made. The images or other third party material in this article are included in the article's Creative Commons licence, unless indicated otherwise in a credit line to the material. If material is not included in the article's Creative Commons licence and your intended use is not permitted by statutory regulation or exceeds the permitted use, you will need to obtain permission directly from the copyright holder. To view a copy of this licence, visit <http://creativecommons.org/licenses/by/4.0/>.

References

1. Hoh CK. Clinical use of FDG PET. *Nucl Med Biol.* 2007;34:737–742. no. 7
2. Khalil MM. Basic science of PET imaging. 2017. Springer.
3. Weber WA, Schwaiger M, Avril N. Quantitative assessment of tumor metabolism using FDG-PET imaging. *Nucl Med Biol.* 2000;27:683–7. no.7
4. Peck M, Pollack H, Friesen A, Muzi M, Shoner S, Shankland E, Fink J, Armstrong J, Link J, Krohn K. Applications of PET imaging with the proliferation marker [^{18}F]-FLT. The quarterly journal of nuclear medicine and molecular imaging: official publication of the Italian Association of Nuclear Medicine (AIMN)[and] the International Association of Radiopharmacology (IAR).[and] Section of the Society of...., 2015;59:95
5. Kaufmann PA, Gnecci-Ruscione T, Yap JT, Rimoldi O, Camici PG. Assessment of the reproducibility of baseline and hyperemic

- myocardial blood flow measurements with ¹⁵O-labeled water and PET. *J Nucl Med.* 1999;40:1848–56. no. 11
6. Gunn RN, Lammertsma AA, Hume SP, Cunningham VJ. Parametric imaging of ligand-receptor binding in PET using a simplified reference region model. *Neuroimage.* 1997;6:279–287. no. 4
 7. Thie JA. Understanding the standardized uptake value, its methods, and implications for usage. *J Nucl Med.* 2004;45:1431–34. no. 9
 8. Tomasi G, Turkheimer F, Aboagye E. Importance of quantification for the analysis of PET data in oncology: review of current methods and trends for the future. *Mol Immunol.* 2012;14:131–46.
 9. Wijngaarden JE, Huisman MC, Jauw YW, van Dongen GA, Greuter HN, Schuit RC, Cleveland M, Gootjes EC, Vugts DJ, Menke-van der Houven van Oordt CW, et al. Validation of simplified uptake measures against dynamic Patlak Ki for quantification of lesional ⁸⁹Zr-immuno-PET antibody uptake. *Eur J Nucl Med Mol Imaging.* 2023;1–9
 10. Vandenberghe S, Mikhaylova E, D’Hoe E, Mollet P, Karp JS. Recent developments in time-of-flight PET. *EJNMMI physics.* 2016;3:1–30. no. 1
 11. Lecomte R. Novel detector technology for clinical PET. *Eur J Nucl Med Mol Imaging.* 2009;36:69–85. no. 1
 12. Zaidi H, Alavi A. Current trends in PET and combined (PET/CT and PET/MR) systems design. *PET clinics.* 2007;2:109–123. no. 2
 13. Lau J, Rousseau E, Kwon D, Lin K-S, Bénard F, Chen X. Insight into the development of PET radiopharmaceuticals for oncology. *Cancers.* 2020;12:1312. no. 5
 14. Vardi Y, Shepp LA, Kaufman L. A statistical model for positron emission tomography. *J Am Stat Assoc.* 1985;80:8–20. no. 389
 15. Leahy RM, Qi J. Statistical approaches in quantitative positron emission tomography. *Statistics and Computing.* 2000;10:147–165. no. 2
 16. Muzi M, O’Sullivan F, Mankoff DA, Doot RK, Pierce LA, Kurland BF, Linden HM, Kinahan PE. Quantitative assessment of dynamic PET imaging data in cancer imaging. *Magn Reson Imaging.* 2012;30:1203–1215. no. 9
 17. Wang G, Rahmim A, Gunn RN. PET parametric imaging: past, present, and future. *IEEE Transactions on Radiation and Plasma Medical Sciences.* 2020;4:663–675. no. 6
 18. Nutt R. The history of positron emission tomography. *Mol Imaging Biol.* 2002;4:11–26. no. 1
 19. Wacholtz EH. History and development of PET. ECEI. 2011. CEwebsitesources. <http://www.cewebsitesources.com/coursePDFs/historyofPET.pdf> (page consultée le 22 Février 2012)
 20. Jones T, and Townsend DW. History and future technical innovation in positron emission tomography. *J Med Imaging.* 2017;4:011013. no. 1
 21. Katal S, Eibschutz LS, Saboury B, Gholamrezanezhad A, Alavi A. Advantages and applications of total-body PET scanning. *Diagnostics.* 2022;12:426. no. 2
 22. Rahmim A, Lodge MA, Karakatsanis NA, Panin VY, Zhou Y, McMillan A, Cho S, Zaidi H, Casey ME, Wahl RL. Dynamic whole-body PET imaging: principles, potentials and applications. *Eur J Nucl Med Mol Imaging.* 2019;46:501–518. no. 2
 23. Badawi RD, Shi H, Hu P, Chen S, Xu T, Price PM, Ding Y, Spencer BA, Nardo L, Liu W, et al. First human imaging studies with the explorer total-body PET scanner. *J Nucl Med.* 2019;60:299–303. no. 3
 24. Pantel AR, Viswanath V, Daube-Witherspoon ME, Dubroff JG, Muehllehner G, Parma MJ, Pryma DA, Schubert EK, Mankoff DA, Karp JS. PennPET explorer: human imaging on a whole-body imager. *J Nucl Med.* 2020;61:144–151. no. 1
 25. Alberts I, Hünermund J-N, Prenosil G, Mingels C, Bohn KP, Viscione M, Sari H, Vollnberg B, Shi K, Afshar-Oromieh A, et al. Clinical performance of long axial field of view PET/CT: a head-to-head intra-individual comparison of the Biograph Vision Quadra with the biograph vision PET/CT. *Eur J Nucl Med Mol Imaging.* 2021;48:2395–2404. no. 8
 26. Spencer BA, Berg E, Schmall JP, Omidvari N, Leung EK, Abdelhafez YG, Tang S, Deng Z, Dong Y, Lv Y, et al. Performance evaluation of the uEXPLORER total-body PET/CT scanner based on NEMA NU 2-2018 with additional tests to characterize PET scanners with a long axial field of view. *J Nucl Med.* 2021;62:861–870. no. 6
 27. Surti S, Viswanath V, Daube-Witherspoon ME, Conti M, Casey ME, Karp JS. Benefit of improved performance with state-of-the-art digital PET/CT for lesion detection in oncology. *J Nucl Med.* 2020;61:1684–90. no. 11
 28. Prenosil GA, Sari H, Fürstner M, Afshar-Oromieh A, Shi K, Rominger A, Hentschel M. Performance characteristics of the Biograph Vision Quadra PET/CT system with a long axial field of view using the NEMA NU 2-2018 standard. *J Nucl Med.* 2022;63:476–484. no. 3
 29. Liu G, Yu H, Shi D, Hu P, Hu Y, Tan H, Zhang Y, Yin H, Shi H. Short-time total-body dynamic pet imaging performance in quantifying the kinetic metrics of ¹⁸F-FDG in healthy volunteers. *Eur J Nucl Med Mol Imaging.* 2021. p. 1–11.
 30. Hu P, Zhang Y, Yu H, Chen S, Tan H, Qi C, Dong Y, Wang Y, Deng Z, Shi H. Total-body ¹⁸F-FDG PET/CT scan in oncology patients: how fast could it be?. *Eur J Nucl Med Mol Imaging.* 2021;48:2384–94. no. 8
 31. Chen Z, Cheng Z, Duan Y, Zhang Q, Zhang N, Gu F, Wang Y, Zhou Y, Wang H, Liang D, Zheng H, Hu Z. Accurate total-body Ki parametric imaging with shortened dynamic ¹⁸F-FDG PET scan durations via effective data processing. *Med Phys.* aug 2022.
 32. Wu Y, Feng T, Shen Y, Fu F, Meng N, Li X, Xu T, Sun T, Gu F, Wu Q, et al. Total-body parametric imaging using the Patlak model: feasibility of reduced scan time. *Med Phys.* 2022.
 33. Viswanath V, Sari H, Pantel AR, Conti M, Daube-Witherspoon ME, Mingels C, Alberts I, Eriksson L, Shi K, Rominger A, et al. Abbreviated scan protocols to capture ¹⁸F-FDG kinetics for long axial FOV PET scanners. *Eur J Nucl Med Mol Imaging.* 2022. pp. 1–11.
 34. Sari H, Eriksson L, Mingels C, Alberts I, Casey ME, Afshar-Oromieh A, Conti M, Cumming P, Shi K, Rominger A. Feasibility of using abbreviated scan protocols with population-based input functions for accurate kinetic modeling of [¹⁸F]-FDG datasets from a long axial FOV PET scanner. *Eur J Nucl Med Mol Imaging.* 2022. p. 1–9.
 35. Liu G, Hu P, Yu H, Tan H, Zhang Y, Yin H, Hu Y, Gu J, Shi H. Ultra-low-activity total-body dynamic PET imaging allows equal performance to full-activity PET imaging for investigating kinetic metrics of ¹⁸F-FDG in healthy volunteers. *Eur J Nucl Med Mol Imaging.* 2021;48:2373–83. no. 8
 36. Tan H, Cai D, Sui X, Qi C, Mao W, Zhang Y, Liu G, Yu H, Chen S, Hu P, et al. Investigating ultra-low-dose total-body [¹⁸F]-FDG PET/CT in colorectal cancer: initial experience. *Eur J Nucl Med Mol Imaging.* 2022;49:1002–11. no. 3
 37. Zhao Y-M, Li Y-H, Chen T, Zhang W-G, Wang L-H, Feng J, Li C, Zhang X, Fan W, Hu Y-Y. Image quality and lesion detectability in low-dose pediatric ¹⁸F-FDG scans using total-body PET/CT. *Eur J Nucl Med Mol Imaging.* 2021;48:3378–85. no. 11
 38. Sachpekidis C, Pan L, Kopp-Schneider A, Weru V, Hassel JC, Dimitrakopoulou-Strauss A. Application of the long axial field-of-view PET/CT with low-dose [¹⁸F] FDG in melanoma. *Eur J Nucl Med Mol Imaging.* 2022. p. 1–10.
 39. Tan H, Gu Y, Yu H, Hu P, Zhang Y, Mao W, Shi H. Total-body PET/CT: current applications and future perspectives. *Am J Roentgenol.* 2020;215:325–337. no. 2

40. Slart RH, Tsoumpas C, Glaudemans AW, Noordzij W, Willemsen A, Borra RJ, Dierckx RA, Lammertsma AA. Long axial field of view PET scanners: a road map to implementation and new possibilities. *Eur J Nucl Med and Mol Imaging*. 2021;48:4236–45. no. 13
41. Alavi A, Saboury B, Nardo L, Zhang V, Wang M, Li H, Raynor WY, Werner TJ, Høiland-Carlsen PF, Revheim M-E. Potential and most relevant applications of total body PET/CT imaging. *Clin Nucl Med*. 2022;47:43–55. no. 1
42. Nadig V, Herrmann K, Mottaghy FM, Schulz V. Hybrid total-body PET scanners—current status and future perspectives. *Eur J Nucl Med and Mol Imaging*. 2021. p. 1–15.
43. Viswanath V, Chitalia R, Pantel AR, Karp JS, Mankoff DA. Analysis of four-dimensional data for total body pet imaging. *PET clinics*. 2021;16:55–64. no. 1
44. Filippi L, Dimitrakopoulou-Strauss A, Evangelista L, Schillaci O. Long axial field-of-view PET/CT devices: are we ready for the technological revolution? 2022.
45. Lammertsma AA. Forward to the past: the case for quantitative PET imaging. *J Nucl Med*. 2017;58:1019–24. no. 7
46. Mankoff DA, Pantel AR, Viswanath V, Karp JS. Advances in PET diagnostics for guiding targeted cancer therapy and studying in vivo cancer biology. *Current Pathobiology Reports*. 2019; 7:97–108. no. 3
47. Zaidi H, Karakatsanis N. Towards enhanced PET quantification in clinical oncology. *Br J Radiol*. 2017;91:20170508. no. 1081
48. Gunn RN, Gunn SR, Cunningham VJ. Positron emission tomography compartmental models. *J Cereb Blood Flow Metab*. 2001;21:635–652. no. 6
49. Bertoldo A, Rizzo G, Veronese M. Deriving physiological information from PET images: from SUV to compartmental modelling. *Clin Transl Imaging*. 2014;2:239–251. no. 3
50. Veronese M, Rizzo G, Bertoldo A, Turkheimer FE. Spectral analysis of dynamic PET studies: a review of 20 years of method developments and applications. *Computational and Mathematical Methods in Medicine*. 2016;2016.
51. Dimitrakopoulou-Strauss A, Pan L, Sachpekidis C. Kinetic modeling and parametric imaging with dynamic PET for oncological applications: general considerations, current clinical applications, and future perspectives. *Eur J Nucl Med Mol Imaging*. 2021;48:21–39. no. 1
52. Pantel AR, Viswanath V, Muzi M, Doot RK, Mankoff DA. Principles of tracer kinetic analysis in oncology, part i: principles and overview of methodology. *J Nucl Med*. 2022;63:342–352. no. 3
53. Lan X, Huo L, Li S, Wang J, Cai W. State-of-the-art of nuclear medicine and molecular imaging in China: after the first 66 years (1956–2022). 2022. p. 1–7.
54. Wang G, Nardo L, Jones T, Cherry SR, Badawi RD. Total-body pet multiparametric imaging of cancer using a voxel-wise strategy of compartmental modeling. *J Nucl Med*. 2021.
55. van Sluis J, van Snick JH, Brouwers AH, Noordzij W, Dierckx RAJO, Borra RJH, Lammertsma AA, Glaudemans AWJM, Slart RHJA, Yaqub M, Tsoumpas C, Boellaard R. Shortened duration whole body 18F-FDG PET Patlak imaging on the Biograph Vision Quadra PET/CT using a population-averaged input function. *EJNMMI Physics*. 2022;9. no. 1
56. Chen R, Yang X, Yu X, Zhou X, Ng YL, Zhao H, Li L, Huang G, Zhou Y, Liu J. Tumor-to-blood ratio for assessment of fibroblast activation protein receptor density in pancreatic cancer using [68ga]Ga-FAPI-04. *Eur J Nucl Med Mol Imaging*. 2022.
57. Chen R, Yang X, Ng YL, Yu X, Huo Y, Xiao X, Zhang C, Chen Y, Zheng C, Li L, et al. First total-body kinetic modeling and parametric imaging of dynamic 68Ga-FAPI-04 PET in pancreatic and gastric cancer. *J Nucl Med*. 2023.
58. Liu G, Mao W, Yu H, Hu Y, Gu J, Shi H. One-stop [18F] FDG and [68Ga] Ga-DOTA-FAPI-04 total-body PET/CT examination with dual-low activity: a feasibility study. *Eur J Nucl Med Mol Imaging*. 2023;1–11.
59. Andersen TL, Andersen FL, Larsson HB, Haddock B, Shah V, Fischer BM, Højgaard L, Law I, Ulrich L. Quantitative image derived input function from long axial field of view scanners. PSMR-TBP 9th Conference on PET/MR and SPECT/MR & Total-body PET workshop. 2022. p. 9.
60. Omidvari N, Jones T, Price PM, Ferre AL, Lu J, Abdelhafez YG, Sen F, Cohen SH, Schmiedehausen K, Badawi RD, et al. First-in-human immunoPET imaging of COVID-19 convalescent patients using dynamic total-body PET and a CD8-targeted mini-body. medRxiv. 2023.
61. Omidvari N, Jones T, Price P, Sen F, Shacklett B, Cohen S, Badawi R, Wilson I, Cherry S. Total-body imaging of CD8+ T cells in patients recovering from COVID-19 - a pilot study using the uEXPLORER total-body PET. *J Nucl Med*. 2022;63(Suppl 2):2327–2327.
62. Abdelhafez Y, Azghadi S, Spencer B, Evans C, Valicenti R, Parikh M, Verma R, Dall’Era M, Foster C, Hagge R, Sen F, Cherry S, Badawi R, Nardo L. Detection rates from 18f-fluciclovine total-body PET/CT in prostate cancer patients with biochemical recurrence. *J Nucl Med*. 2022;63 Suppl 2:3042–3042.
63. Li J, Ni B, Yu X, Wang C, Li L, Zhou Y, Gu Y, Huang G, Hou J, Liu J, et al. Metabolic kinetic modeling of [11c] methionine based on total-body PET in multiple myeloma. *Eur J Nucl Med Mol Imaging*. 2023;1–9.
64. Zhang X, Xie Z, Berg E, Judenhofer M S, Liu W, Xu T, Ding Y, Lv Y, Dong Y, Deng Z, et al. Total-body dynamic reconstruction and parametric imaging on the uEXPLORER. *J Nucl Med*. 2020;61:285–291. no. 2
65. Tan H, Qi C, Cao Y, Cai D, Mao W, Yu H, Sui X, Liu G, Shi H. Ultralow-dose [18F] FDG PET/CT imaging: demonstration of feasibility in dynamic and static images. *Eur Radiol*. 2023;1–11.
66. Liu G, Xu H, Hu P, Tan H, Zhang Y, Yu H, Li X, Shi H. Kinetic metrics of 18F-FDG in normal human organs identified by systematic dynamic total-body positron emission tomography. *Eur J Nucl Med Mol Imaging*. 2021;48:2363–72. no. 8
67. Lv J, Yin H, Yu H, Liu G, Shi H. The feasibility of ultralow-activity 18F-FDG dynamic PET imaging in lung adenocarcinoma patients through total-body PET/CT scanner. *Ann Nucl Med*. 2022;36:887–896. no. 10
68. Yin H, Liu G, Hu Y, Xiao J, Mao W, Lv J, Yu H, Lin Q, Cheng D, Shi H, et al. Dynamic total-body PET/CT imaging reveals kinetic distribution of 68 Ga-DOTATATE in normal organs. *Contrast Media & Molecular Imaging*. 2023;2023
69. Wu Y, Feng T, Zhao Y, Xu T, Fu F, Huang Z, Meng N, Li H, Shao F, Wang M. Whole-body parametric imaging of 18F-FDG PET using uEXPLORER with reduced scanning time. *J Nucl Med*. 2022;63:622–8. no. 4
70. Wang Z, Wu Y, Li X, Bai Y, Chen H, Ding J, Shen C, Hu Z, Liang D, Liu X, Zheng H, Yang Y, Zhou Y, Wang M, Sun T. Comparison between a dual-time-window protocol and other simplified protocols for dynamic total-body 18F-FDG PET imaging. *EJNMMI Physics*. 2022;9. no. 1
71. Huang Z, Wu Y, Fu F, Meng N, Gu F, Wu Q, Zhou Y, Yang Y, Liu X, Zheng H, et al. Parametric image generation with the uEXPLORER total-body PET/CT system through deep learning. *Eur J Nucl Med Mol Imaging*. 2022;1–11.
72. Wang Y, Spencer BA, Schmall J, Li E, Badawi RD, Jones T, Cherry SR, Wang G. High-temporal-resolution lung kinetic modeling using total-body dynamic PET with time-delay and dispersion corrections. *J Nucl Med*. 2023.
73. Li EJ, Spencer BA, Schmall JP, Abdelhafez Y, Badawi RD, Wang G, Cherry SR. Efficient delay correction for total-body PET kinetic modeling using pulse timing methods. *J Nucl Med*. 2022;63:1266–73. no. 8

74. Wang Y, Nardo L, Spencer B, Abdelhafez Y, Chaudhari A, Badawi R, Cherry S, Wang G. Multi-organ metabolic changes in COVID-19 recovery measured with total-body dynamic 18F-FDG PET. *J Nucl Med.* 2022;63(Suppl 2):2329–2329.
75. Li E, Spencer B, Abdelhafez Y, López J, Wang G, Cherry S. Total-body perfusion imaging using [11C]-butanol. *J Nucl Med.* 2022;63(Suppl 2):2247–2247.
76. Wang D, Zhang X, Liu H, Qiu B, Liu S, Zheng C, Fu J, Mo Y, Chen N, Zhou R, Chu C, Liu F, Guo J, Zhou Y, Zhou Y, Fan W, Liu H. Assessing dynamic metabolic heterogeneity in non-small cell lung cancer patients via ultra-high sensitivity total-body [18F]FDG PET/CT imaging: quantitative analysis of [18F]FDG uptake in primary tumors and metastatic lymph nodes. *Eur J Nucl Med Mol Imaging.* 2022;49:4692–4704. no. 13
77. Viswanath V, Pantel AR, Daube-Witherspoon ME, Doot R, Muzi M, Mankoff DA, Karp JS. Quantifying bias and precision of kinetic parameter estimation on the PennPET explorer, a long axial field-of-view scanner. *IEEE Transactions on Radiation and Plasma Medical Sciences.* 2020;4:735–749. no. 6
78. Sari H, Mingels C, Alberts I, Hu J, Buesser D, Shah V, Schepers R, Caluori P, Panin V, Conti M, et al. First results on kinetic modelling and parametric imaging of dynamic 18F-FDG datasets from a long axial FOV PET scanner in oncological patients. *Eur J Nucl Med and Mol Imaging.* 2022;1–13.
79. Sari H, Eriksson L, Mingels C, Alberts I, Casey ME, Afshar-Oromieh A, Conti M, Cumming P, Shi K, Rominger A. Feasibility of using abbreviated scan protocols with population-based input functions for accurate kinetic modeling of [18F]-FDG datasets from a long axial FOV PET scanner. *Eur J Nucl Med Mol Imaging.* 2022.
80. Caobelli F, Seibel S, Krieger K, Bregenzer C, Viscione M, Silva Mendes AF, Sari H, Mercolli L, Afshar-Oromieh A, Rominger A. First-time rest-stress dynamic whole-body 82Rb-PET imaging using a long axial field-of-view PET/CT scanner. *Eur J Nucl Med Mol Imaging.* 2023;1–3.
81. Zhang X, Cherry SR, Xie Z, Shi H, Badawi RD, Qi J. Subsecond total-body imaging using ultrasensitive positron emission tomography. *Proc Natl Acad Sci.* 2020;117:2265–67. no. 5
82. Feng T, Zhao Y, Shi H, Li H, Zhang X, Wang G, Badawi RD, Price PM, Jones T, Cherry SR. The effects of delay on the input function for early dynamics in total body parametric imaging. In: *IEEE Nuclear Science Symposium and Medical Imaging Conference (NSS/MIC).* IEEE. 2019;2019:1–6.
83. Feng T, Zhao Y, Shi H, Li H, Zhang X, Wang G, Price PM, Badawi RD, Cherry SR, Jones T. Total-body quantitative parametric imaging of early kinetics of 18F-FDG. *J Nucl Med.* 2021;62:738–744. no. 5
84. Wu Q, Gu F, Wu Y, Zhou Y, Wang M. Assessment of compartmental models and delay estimation schemes for dynamic total-body PET imaging using uEXPLORER. *J Nucl Med.* 2022;63(Suppl 2):3186–3186.
85. Wang Y, Li E, Cherry SR, Wang G. Total-body pet kinetic modeling and potential opportunities using deep learning. *PET clinics.* 2021;16:613–625. no. 4
86. Gu F, Wu Q, Wu J, Hu D, Xu T, Cao S, Zhou Y, Shi H. Feasibility of standard and generalized Patlak models for dynamic imaging of multiple organs using the uEXPLORER PET scanner. *J Nucl Med.* 2022;63(Suppl 2):3185–3185.
87. Meikle SR, Sossi V, Roncali E, Cherry SR, Banati R, Mankoff D, Jones T, James M, Sutcliffe J, Ouyang J, et al. Quantitative PET in the 2020s: a roadmap. *Phys Med Biol.* 2021;66:06RM01. no. 6
88. Gu F. Improved statistical quantitation of dynamic PET scans. Ph.D. dissertation, University College Cork. 2023.
89. Mankoff DA, Dunnwald LK, Gralow JR, Ellis GK, Charlop A, Lawton TJ, Schubert EK, Tseng J, Livingston RB. Blood flow and metabolism in locally advanced breast cancer: relationship to response to therapy. *J Nucl Med.* 2002;43:500–9. no. 4
90. Dunnwald LK, Doot RK, Specht JM, Gralow JR, Ellis GK, Livingston RB, Linden HM, Gadi VK, Kurland BF, Schubert EK, et al. PET tumor metabolism in locally advanced breast cancer patients undergoing neoadjuvant chemotherapy: value of static versus kinetic measures of fluorodeoxyglucose uptake. *Clin Cancer Res.* 2011;17:2400–09. no. 8
91. Lin Y, Liu E-t, Mou T. Statistical characteristics of 3-D PET imaging: a comparison between conventional and total-body PET scanners. In: *Pattern Recognition and Computer Vision: 5th Chinese Conference, PRCV 2022, Shenzhen, China, November 4–7, 2022, Proceedings, Part II.* Springer; 2022. p. 240–250.
92. Dai B, Daube-Witherspoon ME, McDonald S, Werner ME, Parma MJ, Geagan MJ, Viswanath V, Karp JS. Performance evaluation of the PennPET explorer with expanded axial coverage. *Phys Med Biol.* 2023;68:095007. no. 9
93. O'Sullivan F. Imaging radiotracer model parameters in PET: a mixture analysis approach. *IEEE Trans Med Imaging.* 1993;12:399–412. no. 3
94. Pedersen F, Bergströme M, Bengtsson E, Långström B. Principal component analysis of dynamic positron emission tomography images. *Eur J Nucl Med.* 1994;21:1285–92. no. 12
95. Ahn J, Seo K, Lee J, Lee D. Factor analysis for the quantification of renal cortical blood flow using O-15 water dynamic PET. In: *2000 IEEE Nuclear Science Symposium. Conference Record (Cat. No. 00CH37149).* IEEE. 2000;3:18–153.
96. Wong K-P, Feng D, Meikle SR, Fulham MJ. Segmentation of dynamic PET images using cluster analysis. *IEEE Trans Nucl Sci.* 2002;49:200–7. no. 1
97. Razifar P. Novel approaches for application of principal component analysis on dynamic PET images for improvement of image quality and clinical diagnosis. Ph.D. dissertation, Acta Universitatis Upsaliensis; 2005.
98. Zanderigo F, Parsey RV, Ogden RT. Model-free quantification of dynamic PET data using nonparametric deconvolution. *J Cereb Blood Flow Metab.* 2015;35:1368–79. no. 8
99. Matsubara K, Ibaraki M, Nemoto M, Watabe H, Kimura Y. A review on AI in PET imaging. *Ann Nucl Med.* 2022;1–11.
100. Cheng Z, Wen J, Huang G, Yan J. Applications of artificial intelligence in nuclear medicine image generation. *Quantitative Imaging in Medicine and Surgery.* 2021;11:2792. no. 6
101. Apostolopoulos ID, Papathanasiou ND, Apostolopoulos D J, Panayiotakis GS. Applications of generative adversarial networks (GANs) in positron emission tomography (PET) imaging: a review. *Eur J Nucl Med Mol Imaging.* 2022;1–23.
102. Meier P, Zierler KL. On the theory of the indicator-dilution method for measurement of blood flow and volume. *J Appl Physiol.* 1954;6:731–744. no. 12
103. Chen BC, Huang S-C, Germano G, Kuhle W, Hawkins RA, Buxton D, Brunken RC, Schelbert HR, Phelps ME. Noninvasive quantification of hepatic arterial blood flow with nitrogen-13-ammonia and dynamic positron emission tomography. *J Nucl Med.* 1991;32:2199–2206. no. 12
104. Slimani L, Kudomi N, Oikonen V, Jarvisalo M, Kiss J, Naum A, Borra R, Viljanen A, Sipila H, Ferrannini E, Savunen T, Nuutila P, Iozzo P. Quantification of liver perfusion with [15O]H₂O-PET and its relationship with glucose metabolism and substrate levels. *J Hepatol.* 2008;48:974–982. no. 6 [Online]. Available: <https://www.sciencedirect.com/science/article/pii/S0168827808001335>
105. Materne R, Van Beers BE, Smith AM, Leconte I, Jamart J, Dehoux J-P, Keyeux A, Horsmans Y. Non-invasive quantification of liver perfusion with dynamic computed tomography and a dual-input one-compartmental model. *Clin Sci.* 2000;99:517–525. 11 no. 6. [Online] Available: <https://doi.org/10.1042/cs0990517>

106. Chen S, Feng D. Noninvasive quantification of the differential portal and arterial contribution to the liver blood supply from PET measurements using the/SUP 11C/acetate kinetic model. *IEEE Trans Biomed Eng.* 2004;51:1579–85. no. 9
107. Keiding S. Bringing physiology into PET of the liver. *J Nucl Med.* 2012;53:425–433. no. 3
108. Wang G, Corwin MT, Olson KA, Badawi RD, Sarkar S. Dynamic PET of human liver inflammation: impact of kinetic modeling with optimization-derived dual-blood input function. *Phys Med Biol.* 2018;63:155004. no. 15
109. Wang J, Shao Y, Liu B, Wang X, Geist BK, Li X, Li F, Zhao H, Hacker M, Ding H. et al. Dynamic 18F-FDG PET imaging of liver lesions: evaluation of a two-tissue compartment model with dual blood input function. *BMC Med Imaging.* 2021;21:90. no. 1
110. Svensson P-E, Olsson J, Engbrant F, Bengtsson E, Razifar P. Characterization and reduction of noise in dynamic PET data using masked volumewise principal component analysis. *J Nucl Med Technol.* 2011;39:27–34. no. 1
111. Feng DD, Chen K, Wen L. Noninvasive input function acquisition and simultaneous estimations with physiological parameters for PET quantification: a brief review. *IEEE Transactions on Radiation and Plasma Medical Sciences.* 2020;4:676–683. no. 6
112. van der Weijden CW, Mossel P, Bartels AL, Dierckx RA, Luurtsema G, Lammertsma AA, Willemsen AT, de Vries EF. Non-invasive kinetic modelling approaches for quantitative analysis of brain PET studies. *Eur J Nucl Med Mol Imaging.* 2023;1–15.
113. Graham MM, Lewellen BL. High-speed automated discrete blood sampling for positron emission tomography. *J Nucl Med.* 1993;34:1357–60. no. 8
114. Chen X, Zhang S, Zhang J, Chen L, Wang R, Zhou Y. Noninvasive quantification of nonhuman primate dynamic 18F-FDG PET imaging. *Phys Med Biol.* 2021;66:064005. no. 6
115. Feng T, Tsui BM, Li X, Vranesic M, Lodge MA, Gulaldi NC, Szabo Z. Image-derived and arterial blood sampled input functions for quantitative PET imaging of the angiotensin II subtype 1 receptor in the kidney. *Med Phys.* 2015;42:6736–44. no. 11.
116. Sari H, Erlandsson K, Marner L, Law I, Larsson HB, Thielemans K, Ourselin S, Arridge S, Atkinson D, Hutton BF. Non-invasive kinetic modelling of PET tracers with radiometabolites using a constrained simultaneous estimation method: evaluation with 11C-SB201745. *EJNMMI research.* 2018;8:1–12. no. 1
117. Napieczynska H, Kolb A, Katiyar P, Tonietto M, Ud-Dean M, Stumm R, Herfert K, Calaminus C, Pichler BJ. Impact of the arterial input function recording method on kinetic parameters in small-animal PET. *J Nucl Med.* 2018;59:1159–64. no. 7
118. Chen K, Reiman E, Lawson M, Feng D, Huang S-C. Decay correction methods in dynamic PET studies. *IEEE Trans Nucl Sci.* 1995;42:2173–79. no. 6
119. Bober R. Decay correction for quantitative myocardial PET perfusion in established PET scanners: a potentially overlooked source of errors. *J Nucl Med Technol.* 2021;49:344–9. no. 4
120. Votaw JR, Shulman SD. Performance evaluation of the Pico-Count flow-through detector for use in cerebral blood flow PET studies. *J Nucl Med.* 1998;39:509–515. no. 3
121. Berezhkovskiy LM, Zhang X, Cheong J. A convenient method to measure blood–plasma concentration ratio using routine plasma collection in *in vivo* pharmacokinetic studies. *J Pharm Sci.* 2011;100:5293–98. no. 12
122. Li F, Hicks JW, Yu L, Desjardin L, Morrison L, Hadway J, Lee T-Y. Plasma radio-metabolite analysis of PET tracers for dynamic PET imaging: Tlc and autoradiography. *EJNMMI research.* 2020;10:1–12. no. 1
123. Gunn RN, Sargent PA, Bench CJ, Rabiner EA, Osman S, Pike VW, Hume SP, Grasby PM, Lammertsma AA. Tracer kinetic modeling of the 5-Ht1A receptor ligand [carbonyl-11C] WAY-100635 for PET. *Neuroimage.* 1998;8:426–440. no. 4
124. Asselin M-C, Montgomery AJ, Grasby PM, Hume SP. Quantification of PET studies with the very high-affinity dopamine D2/D3 receptor ligand [11C] FLB 457: re-evaluation of the validity of using a cerebellar reference region. *J Cereb Blood Flow Metab.* 2007;27:378–392. no. 2
125. Watabe H, Channing MA, Der MG, Adams HR, Jagoda E, Herscovitch P, Eckelman WC, Carson RE. Kinetic analysis of the 5-Ht2A ligand [11C] MDL 100,907. *J Cereb Blood Flow Metab.* 2000;20:899–909. no. 6
126. Meyer PT, Elmenhorst D, Bier D, Holschbach MH, Matusch A, Coenen HH, Zilles K, Bauer A. Quantification of cerebral α_1 adenosine receptors in humans using [18F] CPFPPX and PET: an equilibrium approach. *Neuroimage.* 2005;24:1192–1204. no. 4
127. Huang S, Barrio J, Yu D, Chen B, Grafton S, Melega W, Hoffman J, Satyamurthy N, Mazziotta J, Phelps M. Modelling approach for separating blood time activity curves in positron emission tomographic studies. *Phys Med Biol.* 1991;36:749. no. 6
128. Tonietto M, Rizzo G, Veronese M, Fujita M, Zoghbi SS, Zanotti-Fregonara P, Bertoldo A. Plasma radiometabolite correction in dynamic PET studies: insights on the available modeling approaches. *J Cereb Blood Flow Metab.* 2016;36:326–339. no. 2
129. Takikawa S, Dhawan V, Spetsieris P, Robeson W, Chaly T, Dahl R, Margouleff D, Eidelberg D. Noninvasive quantitative fluorodeoxyglucose PET studies with an estimated input function derived from a population-based arterial blood curve. *Radiology.* 1993;188:131–6. no. 1
130. Vriens D, de Geus-Oei L-F, Oyen WJ, Visser EP. A curve-fitting approach to estimate the arterial plasma input function for the assessment of glucose metabolic rate and response to treatment. *J Nucl Med.* 2009;50:1933–39. no. 12
131. Feng D, Huang S-C, Wang X. Models for computer simulation studies of input functions for tracer kinetic modeling with positron emission tomography. *Int J Biomed Comput.* 1993;32:95–110. no. 2
132. Parsey RV, Slifstein M, Hwang D-R, Abi-Dargham A, Simpson N, Mawlawi O, Guo N-N, Van Heertum R, Mann JJ, Laruelle M. Validation and reproducibility of measurement of 5-Ht1A receptor parameters with [carbonyl-11C] WAY-100635 in humans: comparison of arterial and reference tissue input functions. *J Cereb Blood Flow Metab.* 2000;20:1111–33. no. 7
133. Tonietto M, Rizzo G, Veronese M, Bertoldo A. Modelling arterial input functions in positron emission tomography dynamic studies. In: 37th annual international conference of the IEEE Engineering in Medicine and Biology Society (EMBC). *IEEE.* 2015;2015:2247–50.
134. Feng D, Wong K-P, Wu C-M, Siu W-C. A technique for extracting physiological parameters and the required input function simultaneously from PET image measurements: theory and simulation study. *IEEE Trans Inf Technol Biomed.* 1997;1:243–254. no. 4
135. Wong K-P, Feng D, Meikle SR, Fulham MJ. Simultaneous estimation of physiological parameters and the input function-*in vivo* PET data. *IEEE Trans Inf Technol Biomed.* 2001;5:67–76. no. 1
136. Wong K-P, Meikle SR, Feng D, Fulham MJ. Estimation of input function and kinetic parameters using simulated annealing: application in a flow model. *IEEE Trans Nucl Sci.* 2002;49:707–713. no. 3
137. Xiu Z, Muzi M, Huang J, Wolsztynski E. Patient-adaptive population-based modeling of arterial input functions. *IEEE Trans Med Imaging.* 2022.
138. Huang J, O'Sullivan F. An analysis of whole body tracer kinetics in dynamic PET studies with application to image-based blood input function extraction. *IEEE Trans Med Imaging.* 2014;33:1093–1108. no. 5
139. Wu Q, Gu F, Gu Y, Xu T, Zhou Y, Shi H. Impact of equilibration time (t^*) on Patlak quantitation in dynamic total-body

- imaging using the uEXPLORER PET scanner. 2022;63 Suppl 2: 3184–3184.
140. O'Sullivan F, Wu Q, Gu F, Shi K, O'Suilleabhain L, Xue S, Rominger A. Mapping FDG tracer kinetics and their uncertainties via the bootstrap using data from a long-axial FOV PET/CT scanner. *J Nucl Med.* 2022;63(Suppl 2):3220–3220.
 141. Kety SS, Schmidt CF. The nitrous oxide method for the quantitative determination of cerebral blood flow in man: theory, procedure and normal values. *J Clin Investig.* 1948;27:476–483. no. 4
 142. Mintun MA, Raichle ME, Kilbourn MR, Wooten GF, Welch MJ. A quantitative model for the in vivo assessment of drug binding sites with positron emission tomography. *Annals of Neurology: Official Journal of the American Neurological Association and the Child Neurology Society.* 1984;15:217–227. no. 3
 143. Sokoloff L, Reivich M, Kennedy C, Rosiers MD, Patlak C, Pettigrew Kea, Sakurada O, Shinohara M. The [¹⁴C] deoxyglucose method for the measurement of local cerebral glucose utilization: theory, procedure, and normal values in the conscious and anesthetized Albino rat 1. *J Neurochem.* 1977;28:897–916. no. 5
 144. Phelps M, Huang S, Hoffman E, Selin C, Sokoloff L, Kuhl D. Tomographic measurement of local cerebral glucose metabolic rate in humans with (F-18) 2-fluoro-2-deoxy-d-glucose: validation of method. *Ann Neurol: Off J Am Neurol Assoc Child Neurol Soc.* 1979;6:371–388. no. 5
 145. Huang S-C, Phelps ME, Hoffman EJ, Sideris K, Selin CJ, Kuhl DE. Noninvasive determination of local cerebral metabolic rate of glucose in man. *Am J Physiol Endocrinol Metab.* 1980;238: E69–E82. no. 1
 146. Trench WF. Elementary differential equations with boundary value problems. 2013.
 147. Keramida G, Potts J, Bush J, Verma S, Dizdarevic S, Peters AM. Accumulation of 18F-FDG in the liver in hepatic steatosis. *Am J Roentgenol.* 2014;203:643–8. no. 3
 148. Patlak CS, Blasberg RG, Fenstermacher JD. Graphical evaluation of blood-to-brain transfer constants from multiple-time uptake data. *J Cereb Blood Flow Metab.* 1983;3:1–7. no. 1
 149. Logan J, Fowler JS, Volkow ND, Wolf AP, Dewey SL, Schlyer DJ, MacGregor RR, Hitzemann R, Bendriem B, Gatley SJ, et al. Graphical analysis of reversible radioligand binding from time—activity measurements applied to [N-11C-methyl]-(-)-cocaine PET studies in human subjects. *J Cereb Blood Flow Metab.* 1990;10:740–7. no. 5
 150. Zhou Y, Ye W, Brašić JR, Wong DF. Multi-graphical analysis of dynamic PET. *Neuroimage.* 2010;49:2947–57. no. 4
 151. Logan J. A review of graphical methods for tracer studies and strategies to reduce bias. *Nucl Med Biol.* 2003;30:833–844. no. 8
 152. Choi Y, Hawkins RA, Huang S-C, Gambhir SS, Brunken RC, Phelps ME, Schelbert HR. Parametric images of myocardial metabolic rate of glucose generated from dynamic cardiac pet and 2-[18F] fluoro-2-deoxy-d-glucose studies. *J Nucl Med Off Publ Soc Nucl Med.* 1991;32:733–8. no. 4
 153. Chen K, Bandy D, Reiman E, Huang S-C, Lawson M, Feng D, Yun L-s, Palant A. Noninvasive quantification of the cerebral metabolic rate for glucose using positron emission tomography, 18f-fluoro-2-deoxyglucose, the Patlak method, and an image-derived input function. *J Cereb Blood Flow Metab.* 1998;18: 716–723. no. 7
 154. Coello C, Fisk M, Mohan D, Wilson FJ, Brown AP, Polkey MI, Wilkinson I, Tal-Singer R, Murphy PS, Cheriyan J, et al. Quantitative analysis of dynamic 18 F-FDG PET/CT for measurement of lung inflammation. *EJNMMI research.* 2017;7:1–12. no. 1
 155. Chen Y, Li L, Yu X, Wang J, Wang Y, Huang G, Liu J. Is dynamic total-body PET imaging feasible in the clinical daily practice? 2021.
 156. Wu Y, Feng T, Zhao Y, Xu T, Fu F, Huang Z, Meng N, Li H, Shao F, Wang M. Whole-body parametric imaging of FDG PET using uEXPLORER with reduced scan time. *J Nucl Med Off Publ Soc Nucl Med.* 2022. p. jnumed–120.
 157. Choi Y, Hawkins RA, Huang S-C, Brunken RC, Hoh CK, Messa C, Nitzsche EU, Phelps ME, Schelbert HR. Evaluation of the effect of glucose ingestion and kinetic model configurations of FDG in the normal liver. *J Nucl Med.* 1994;35:818–823. no. 5
 158. Torizuka T, Tamaki N, Inokuma T, Magata Y, Sasayama S, Yonekura Y, Tanaka A, Yamaoka Y, Yamamoto K, Konishi J. In vivo assessment of glucose metabolism in hepatocellular carcinoma with FDG-PET. *J Nucl Med.* 1995;36:1811–17. no. 10
 159. Patlak CS, Blasberg RG. Graphical evaluation of blood-to-brain transfer constants from multiple-time uptake data. generalizations. *J Cereb Blood Flow Metab.* 1985;5:584–590. no. 4
 160. Karakatsanis NA, Zhou Y, Lodge M A, Casey ME, Wahl RL, Zaidi H, Rahmim A. Generalized whole-body Patlak parametric imaging for enhanced quantification in clinical PET. *Phys Med Biol.* 2015;60:8643. no. 22
 161. Cunningham V J, Jones T. Spectral analysis of dynamic PET studies. *J Cereb Blood Flow Metab.* 1993;13:15–23. no. 1
 162. Turkheimer FE, Hinz R, Gunn RN, Aston JA, Gunn SR, Cunningham VJ. Rank-shaping regularization of exponential spectral analysis for application to functional parametric mapping. *Phys Med Biol.* 2003;48:3819. no. 23
 163. Veronese M, Bertoldo A, Bishu S, Unterman A, Tomasi G, Smith CB, Schmidt KC. A spectral analysis approach for determination of regional rates of cerebral protein synthesis with the L-[1-¹¹C] leucine PET method. *J Cereb Blood Flow Metab.* 2010;30: 1460–76. no. 8
 164. Li Z, Yipintsoi T, Bassingthwaight JB. Nonlinear model for capillary-tissue oxygen transport and metabolism. *Ann Biomed Eng.* 1997;25:604–619. no. 4
 165. King RB, Raymond GM, Bassingthwaight JB. Modeling blood flow heterogeneity. *Ann Biomed Eng.* 1996;24:352–372. no. 3
 166. Østergaard L, Weisskoff RM, Chesler DA, Gyldensted C, Rosen BR. High resolution measurement of cerebral blood flow using intravascular tracer bolus passages. part i: Mathematical approach and statistical analysis. *Magn Reson Med.* 1996;36:715–725. no. 5
 167. Østergaard L, Chesler DA, Weisskoff RM, Sorensen AG, Rosen BR. Modeling cerebral blood flow and flow heterogeneity from magnetic resonance residue data. *J Cereb Blood Flow Metab.* 1999;19:690–9. no. 6
 168. Barrio JR, Huang S-C, Satyamurthy N, Scafoglio CS, Amy SY, Alavi A, Krohn KA. Does 2-FDG PET accurately reflect quantitative in vivo glucose utilization? *J Nucl Med.* 2020;61:931–7. no. 6
 169. O'Sullivan F, Muzi M, Spence AM, Mankoff DM, O'sullivan JN, Fitzgerald N, Newman GC, Krohn KA. Nonparametric residue analysis of dynamic PET data with application to cerebral FDG studies in normals. *J Am Stat Assoc.* 2009;104:556–571. no. 486
 170. Hawe D, Hernández Fernández FR, O'Suilleabháin L, Huang J, Wolsztynski E, O'Sullivan F. Kinetic analysis of dynamic positron emission tomography data using open-source image processing and statistical inference tools. *Wiley Interdiscip Rev Comput Stat.* 2012;4:316–322. no. 3
 171. O'Sullivan F, Muzi M, Mankoff DA, Eary JF, Spence AM, Krohn KA. Voxel-level mapping of tracer kinetics in PET studies: a statistical approach emphasizing tissue life tables. *Ann Appl Stat.* 2014;8:1065. no. 2
 172. Chen Y, Goldsmith J, Ogden RT. Functional data analysis of dynamic PET data. *J Am Stat Assoc.* 2019;114:595–609. no. 526
 173. Gu F, O'Sullivan F, Muzi M, Mankoff DA. Quantitation of multiple injection dynamic pet scans: an investigation of the benefits

- of pooling data from separate scans when mapping kinetics. *Phys Med Biol.* 2021;66:135010. no. 13
174. O'Sullivan F, Gu F, Wu Q, O'Suilleabhain LD. A generalized linear modeling approach to bootstrapping multi-frame PET image data. *Med Image Anal.* 2021. p. 102132.
 175. Gu F, Wu Q, O'Sullivan F. Image-domain bootstrapping of PET time-course data for assessment of uncertainty in complex regional summaries of mapped kinetics. In: *IEEE Nuclear Science Symposium and Medical Imaging Conference (NSS/MIC).* IEEE. 2021;2021:1–3.
 176. Gu F, Wu Q, O'Sullivan F, Huang J, Muzi M, Mankoff DA. An illustration of the use of model-based bootstrapping for evaluation of uncertainty in kinetic information derived from dynamic pet. In: *IEEE Nuclear Science Symposium and Medical Imaging Conference (NSS/MIC).* IEEE. 2019;2019:1–3.
 177. Kotasidis FA, Tsoumpas C, Rahmim A. Advanced kinetic modelling strategies: towards adoption in clinical PET imaging. *Clin Transl Imaging.* 2014;2:219–237. no. 3
 178. Snyder DL. Parameter estimation for dynamic studies in emission-tomography systems having list-mode data. *IEEE Trans Nucl Sci.* 1984;31:925–931. no. 2
 179. Carson RE, Lange K. Comment: the EM parametric image reconstruction algorithm. *J Am Stat Assoc.* 1985;80:20–22. no. 389
 180. Meikle SR, Matthews JC, Cunningham VJ, Bailey DL, Livieratos L, Jones T, Price P. Parametric image reconstruction using spectral analysis of PET projection data. *Phys Med Biol.* 1998;43:651. no. 3
 181. Kamasak ME, Bouman CA, Morris ED, Sauer K. Direct reconstruction of kinetic parameter images from dynamic PET data. *IEEE Trans Med Imaging.* 2005;24:636–650. no. 5
 182. Wang G, Fu L, Qi J. Maximum a posteriori reconstruction of the Patlak parametric image from sinograms in dynamic PET. *Phys Med Biol.* 2008;53:593. no.3
 183. Tsoumpas C, Turkheimer FE, Thielemans K. Study of direct and indirect parametric estimation methods of linear models in dynamic positron emission tomography. *Med Phys.* 2008;35:1299–1309. no. 4
 184. Wang G, Qi J. Generalized algorithms for direct reconstruction of parametric images from dynamic PET data. *IEEE Trans Med Imaging.* 2009;28:1717–1726. no. 11
 185. Rahmim A, Tang J, Zaidi H. Four-dimensional (4D) image reconstruction strategies in dynamic PET: beyond conventional independent frame reconstruction. *Med Phys.* 2009;36:3654–70. no. 8
 186. Wang G, Qi J. Direct estimation of kinetic parametric images for dynamic PET. *Theranostics.* 2013;3:802. no. 10
 187. Li Y, Hu J, Sari H, Xue S, Ma R, Kandarpa S, Visvikis D, Rominger A, Liu H, Shi K. A deep neural network for parametric image reconstruction on a large axial field-of-view PET. *Eur J Nucl Med Mol Imaging.* 2022. p. 1–14.
 188. Karakatsanis NA, Casey ME, Lodge MA, Rahmim A, Zaidi H. Whole-body direct 4D parametric PET imaging employing nested generalized Patlak expectation–maximization reconstruction. *Phys Med Biol.* 2016;61:5456. no. 15
 189. Li W, Liu H, Cheng F, Li Y, Li S, Yan J. Artificial intelligence applications for oncological positron emission tomography imaging. *Eur J Radiol.* 2021;134: 109448.
 190. Zaidi H, El Naqa I. Quantitative molecular positron emission tomography imaging using advanced deep learning techniques. *Annu Rev Biomed Eng.* 2021;23:249–76.
 191. Gong K, Guan J, Kim K, Zhang X, Yang J, Seo Y, El Fakhri G, Qi J, Li Q. Iterative PET image reconstruction using convolutional neural network representation. *IEEE Trans Med Imaging.* 2018;38:675–685. no. 3
 192. Reader AJ, Corda G, Mehranian A, da Costa-Luis C, Ellis S, Schnabel JA. Deep learning for PET image reconstruction. *IEEE Transactions on Radiation and Plasma Medical Sciences.* 2020;5:1–25. no. 1
 193. Häggström I, Schmidlein CR, Campanella G, Fuchs TJ. Deep-PET: a deep encoder-decoder network for directly solving the pet image reconstruction inverse problem. *Med Image Anal.* 2019;54:253–62.
 194. Cui J, Gong K, Guo N, Wu C, Meng X, Kim K, Zheng K, Wu Z, Fu L, Xu B, et al. PET image denoising using unsupervised deep learning. *Eur J Nucl Med Mol Imaging.* 2019;46:2780–2789. no. 13
 195. Lu W, Onofrey JA, Lu Y, Shi L, Ma T, Liu Y, Liu C. An investigation of quantitative accuracy for deep learning based denoising in oncological PET. *Phys Med Biol.* 2019;64:165019. no. 16
 196. Niyas S, Pawan S, Kumar MA, Rajan J. Medical image segmentation using 3D convolutional neural networks: a review. 2021. arXiv preprint [arXiv:2108.08467](https://arxiv.org/abs/2108.08467)
 197. Guo Z, Li X, Huang H, Guo N, Li Q. Deep learning-based image segmentation on multimodal medical imaging. *IEEE Transactions on Radiation and Plasma Medical Sciences.* 2019;3:162–169. no. 2
 198. Gong K, Catana C, Qi J, Li Q. Direct reconstruction of linear parametric images from dynamic PET using nonlocal deep image prior. *IEEE Trans Med Imaging.* 2021;41:680–9. no. 3
 199. Zaker N, Haddad K, Faghihi R, Arabi H, Zaidi H. Direct inference of Patlak parametric images in whole-body PET/CT imaging using convolutional neural networks. *Eur J Nucl Med Mol Imaging.* 2022;49:4048–63. no. 12
 200. Wang H, Wu Y, Huang Z, Li Z, Zhang N, Fu F, Meng N, Wang H, Zhou Y, Yang Y, et al. Deep learning–based dynamic pet parametric Ki image generation from lung static PET. *Eur Radiol.* 2022. p. 1–10.
 201. Yao S, Feng T, Zhao Y, Wu R, Wang R, Wu S, Li C, Xu B. Simplified protocol for whole-body Patlak parametric imaging with 18F-FDG PET/CT: feasibility and error analysis. *Med Phys.* 2021;48:2160–2169. no. 5
 202. Dias AH, Pedersen MF, Danielsen H, Munk OL, Gormsen LC. Clinical feasibility and impact of fully automated multiparametric PET imaging using direct Patlak reconstruction: evaluation of 103 dynamic whole-body 18F-FDG PET/CT scans. *Eur J Nucl Med Mol Imaging.* 2021;48:837–850. no. 3
 203. Gu F, Hernandez F, O'Sullivan F, Muzi M, Eyal S, Unadkat J, Mankoff D. Whole-body metabolic imaging of P-glycoprotein activity in pregnant macaques. In: *European Molecular Imaging Meeting.* 2019.
 204. Kuntner C, Stout D. Quantitative preclinical PET imaging: opportunities and challenges. *Frontiers in physics.* 2014;2:12.
 205. Sun T, Wu Y, Wei W, Fu F, Meng N, Chen H, Li X, Bai Y, Wang Z, Ding J, et al. Motion correction and its impact on quantification in dynamic total-body 18f-fluorodeoxyglucose PET. *EJNMMI physics.* 2022;9:1–16. no. 1
 206. Dutta J, Leahy RM, Li Q. Non-local means denoising of dynamic PET images. *PloS one.* 2013;8:e81390. no. 12
 207. Hicks RJ. So, you want to get into “total-body” PET/CT scanning? An installation guide for beginners! *Cancer Imaging.* 2023;23:35. no. 1
 208. Vandenberghe S, Karakatsanis NA, Akl MA, Maebe J, Surti S, Dierckx RA, Pryma DA, Nehmeh SA, Bouhali O, Karp JS. The potential of a medium-cost long axial FOV PET system for nuclear medicine departments. *Eur J Nucl Med Mol Imaging.* 2023;50:652–660. no. 3
 209. Alberts I, Sari H, Mingels C, Afshar-Oromieh A, Pyka T, Shi K, Rominger A. “Long-axial field-of-view PET/CT: perspectives and review of a revolutionary development in nuclear medicine based on clinical experience in over 7000 patients,” *Cancer Imaging.* 2023;23:1–15. no. 1

210. Yu H, Gu Y, Fan W, Gao Y, Wang M, Zhu X, Wu Z, Liu J, Li B, Wu H, et al. Expert consensus on oncological [18F] FDG total-body PET/CT imaging (version 1). *Eur Radiol.* 2023;33:615–626. no. 1
211. Knudsen GM, Ganz M, Appelhoff S, Boellaard R, Bormans G, Carson RE, Catana C, Doudet D, Gee AD, Greve DN, et al. Guidelines for the content and format of PET brain data in publications and archives: a consensus paper. *J Cereb Blood Flow Metab.* 2020;40:1576–1585. no. 8
212. Norgaard M, Matheson GJ, Hansen HD, Thomas A, Searle G, Rizzo G, Veronese M, Giacomel A, Yaqub M, Tonietto M, et al. PET-BIDS, an extension to the brain imaging data structure for positron emission tomography. *Sci Data.* 2022;9:65. no. 1

Publisher's Note Springer Nature remains neutral with regard to jurisdictional claims in published maps and institutional affiliations.